



A Mesoscale Ocean–Atmosphere Coupled Pathway for Decadal Variability of the Kuroshio Extension System

BOLAN GAN¹,^{a,b} TIANYU WANG,^a LIXIN WU,^{a,b} JIANPING LI,^{a,b} BO QIU,^c HAIYUAN YANG,^{a,b} AND LI ZHANG^{a,b}

^a *Frontiers Science Center for Deep Ocean Multispheres and Earth System and Key Laboratory of Physical Oceanography, Ocean University of China, Qingdao, China*

^b *Laoshan Laboratory, Qingdao, China*

^c *Department of Oceanography, University of Hawai'i at Mānoa, Honolulu, Hawaii*

(Manuscript received 20 July 2021, in final form 9 September 2022)

ABSTRACT: The Kuroshio Extension (KE) system has been observed to experience a decadal cycle between dynamically stable and unstable states. However, divergent conclusions on its interaction with the atmosphere obfuscate the understanding of its oscillatory nature at the preferred decadal time scale. Here, using satellite observations and the ERA-Interim reanalysis in 2002–16, physical process-oriented diagnoses suggest that the wintertime finer-scale thermodynamic response to mesoscale oceanic surface conditions and slow oceanic Rossby wave adjustment frame a coupled ocean–atmosphere delayed oscillator for the decadal KE variability. During the stable state of the KE system, the downstream KE transition region is rich in mesoscale oceanic warming associated with warm eddies, which induces surface wind convergence and upward motion, probably via the enhanced turbulent mixing. Meanwhile, increased finer-scale diabatic heating in the lower troposphere with abundant moisture supply from warmer water likely facilitates the deep-reaching updraft that adiabatically cools the middle troposphere. The background northwesterly wind helps to spread out the cooling, leading to southward deflection of local atmospheric eddy available potential energy (EAPE) production by baroclinic conversion. Consequently, the synoptic eddy activity displaces southward across the basin with additional energy supply from the increased diabatic production of EAPE downstream. Anomalous synoptic eddy thermal and vorticity forcing eventually fosters the basin-scale equivalent-barotropic cyclonic circulation anomaly, which is further maintained by energy conversion from the background state. The resultant wind-driven negative sea surface height anomalies propagate westward into the upstream KE region with a delay of ~4 years and can trigger the unstable state of the KE system.

KEYWORDS: Atmosphere-ocean interaction; Eddies; Decadal variability; Storm tracks

1. Introduction

The Kuroshio Extension (KE), as a strong eastward inertial jet after the departure of the Kuroshio from the coast of Japan, is well known for being a complex dynamic system abundant with submesoscale motions, mesoscale eddies, and large meanders (e.g., Mizuno and White 1983; Qiu et al. 1991; Yasuda 2003; Qiu and Chen 2005; Taguchi et al. 2010; Xu et al. 2016; Su et al. 2018). The KE region is also a hot spot for ocean–atmosphere interactions at weather and climate scales (Kwon et al. 2010; Kelly et al. 2010; Czaja et al. 2019). Enormous heat and moisture supplies from warm KE fuel intense storms and atmospheric

fronts, which regulate the large-scale atmospheric circulation and help in shaping mode waters that preserve climate memory in the ocean interior (e.g., Nakamura et al. 2004; Oka and Qiu 2012; Kida et al. 2015; Yu et al. 2020).

It has long been recognized that the KE system exhibits pronounced decadal modulations between the stable and unstable dynamic states (e.g., Qiu and Chen 2005; Taguchi et al. 2007; Ceballos et al. 2009; Sasaki et al. 2013; Pierini 2014; Yang et al. 2018). When the KE system is in the stable state, the jet path is relatively shortened and less convoluted (Y. Seo et al. 2014), and both the KE jet and southern recirculation gyre are stronger than normal. Meanwhile, ocean eddy activity tends to be subdued in the upstream (west of 153°E) but vigorous in the downstream region. Correspondingly, cold SST anomalies are confined to the upstream north of the KE jet, whereas warm anomalies cover the downstream region (Qiu et al. 2017; Yang et al. 2018). The reverse holds when the KE system switches to the unstable state. Since the start of the satellite altimetry era in 1993, the KE system has been observed to experience two stable and unstable cycles. This decadal variability is of great importance to

¹ Denotes content that is immediately available upon publication as open access.

Bolan Gan and Tianyu Wang contributed equally to this work.

Corresponding author: Bolan Gan, gbl0203@ouc.edu.cn

DOI: 10.1175/JCLI-D-21-0557.1

© 2022 American Meteorological Society. For information regarding reuse of this content and general copyright information, consult the AMS Copyright Policy (www.ametsoc.org/PUBSReuseLicenses).

local biogeochemistry, marine ecosystems, and basin-scale climate variability (e.g., Kwon et al. 2010; Qiu and Chen 2011; Nishikawa et al. 2011; Oka et al. 2015, 2019; Joh and Di Lorenzo 2019).

The satellite-observed decadal variability of the KE system is suggested to be associated with wind stress curl variability in the central North Pacific, which drives westward propagation of sea surface height (SSH) anomalies as baroclinic Rossby waves (e.g., Qiu and Chen 2005, 2010; Ceballos et al. 2009; Nonaka et al. 2020) and/or triggers oceanic intrinsic processes that reorganize SSH variability in space (e.g., Taguchi et al. 2007; Sasaki et al. 2013; Pierini 2014). Regarding the relative importance of locally oceanic intrinsic variability and remotely wind-driven variability, Nonaka et al. (2020) suggested that variations of the KE jet speed and the downstream eddy activity on the decadal time scale are largely wind-driven, whereas on the interannual time scale the intrinsic variability takes charge. The decadal change in basinwide wind forcing was suggested to stem from the Pacific decadal oscillation (PDO; e.g., Qiu and Chen 2005, 2010) or the North Pacific Gyre Oscillation (NPGO; e.g., Ceballos et al. 2009; Pierini 2014; Yang et al. 2017), which are two dominant modes of low-frequency climate variability in the North Pacific. However, the PDO and NPGO are linearly correlated to a large extent since the climate regime shift in 1976–77, with $r = -0.53$ (-0.64) between the monthly PDO and NPGO indices during 1979–2018 (1992–2018) after a 13-month running mean, and this obscures the importance of the PDO- versus NPGO-related wind forcing. In fact, the decadal cycle (~ 10 yr) of the KE system did not fit to a ~ 20 -yr oscillation of PDO/NPGO and their lead-lag relationship exhibits an oscillatory feature, hinting that the coupled ocean–atmosphere oscillation likely makes the KE system variations preferred at the decadal time scale. Qiu et al. (2007) demonstrated that the idealized model cannot reproduce the observed decadal spectral peak of sea surface temperature (SST) in the KE region without taking into account the SST feedback to wind stress curl.

In the framework of coupled ocean–atmosphere oscillation, a delayed negative feedback mechanism favoring decadal transition of the KE system from stable to unstable state lies in the positive wind stress curl response over the central-to-eastern basin (Qiu et al. 2014; Joh and Di Lorenzo 2019). However, a fundamental issue remains on how atmosphere remotely responds to the decadal KE variations, since there has been discrepancy in the atmospheric responding patterns across previous statistical studies. For instance, a northward shift of the KE subsurface thermal front was suggested to be followed by weak surface low anomaly over the KE region and strong surface high anomaly over the Bering Sea, akin to the North Pacific Oscillation pattern (Frankignoul et al. 2011), as well as decreased synoptic eddy heat flux over the North Pacific (Kwon and Joyce 2013). However, O'Reilly and Czaja (2015) reported that when the KE jet is accelerated and shifts northward, a stronger KE SST front is associated with a zonal shift of synoptic eddy heat flux (increase/decrease in the western/eastern basin) and a quadrupole structure of large-scale atmospheric circulation anomalies. Révelard et al. (2016) reported that when the KE system is in the stable state, warm SST anomalies dominate the Kuroshio–

Oyashio Extension (KOE) region, which generates a northeastward shift of storm-track activity and an equivalent-barotropic high pressure anomaly over the northwestern basin. But regarding transient atmospheric response to decadal SST variations in the KOE region, Wills and Thompson (2018) found that wintertime warm SST anomalies are followed by an equivalent-barotropic low pressure anomaly that emerges over the KOE and matures into basinwide within a month. Some of those findings with anomalous low pressure response downstream could favor a delayed negative feedback mechanism, but dynamical processes involved in the atmospheric responses have yet hitherto been diagnosed systematically.

Observational evidence is mounting that oceanic fronts and eddies leave their imprints on the marine atmospheric boundary layer (MABL) and further influence the free atmosphere at weather and larger scales (e.g., Chelton and Xie 2010; Frenger et al. 2013; Masunaga et al. 2015; Liu et al. 2018; Wang et al. 2019; L. Zhang et al. 2020; Chen et al. 2020). For instance, in the KE region, mesoscale warm eddies cause acceleration of surface winds and increases in turbulent heat release, water vapor content, and convective rain rate (J. Ma et al. 2015). MABL also deepens over warm eddies, accompanied by ascending motion penetrating into the free atmosphere (Chen et al. 2017). Modeling studies based on high-resolution atmospheric general circulation model (AGCM) experiments suggest that synoptic eddies tend to be more energetic in the presence of the northwestern Pacific subarctic fronts and mesoscale eddies (Smirnov et al. 2015; X. Ma et al. 2015; Kuwano-Yoshida and Minobe 2017; Foussard et al. 2019; C. Zhang et al. 2020), whereas the westerly jet response to mesoscale eddies seems model dependent (Foussard et al. 2019; Cai et al. 2021). Despite the vigorous mesoscale motions embedded in the KE dynamic system, whether their interaction with atmosphere plays a role in the decadal KE variations remains unknown. In the present study, we seek to address this issue by performing process-oriented diagnostics and propose a wintertime mesoscale ocean–atmosphere coupled delayed oscillator paradigm, in which the finer-scale thermodynamic response to mesoscale SST anomalies in the eddy-rich KE region is emphasized.

The rest of the paper is organized as follows. Section 2 briefly describes the datasets and methods. Section 3 presents the oceanic forcing and atmospheric responding patterns associated with decadal variations of the KE system. Section 4 presents diagnostics of dynamical processes underlying the responses of large-scale atmospheric circulation, storm tracks, and MABL. Section 5 investigates the potential feedback of the atmospheric response onto the KE system. Section 6 gives a discussion and summary.

2. Data and methods

a. Satellite observations and ERA-Interim

The dynamical state of KE system is evaluated based on the daily SSH product (Ducet et al. 2000) distributed by the Copernicus Marine and Environment Monitoring Service, which merges all satellite altimeter measurements, available

on 0.25° grid spacing from 1 January 1993 onward. The daily SST data are taken from the Advanced Very High Resolution Radiometer (AVHRR)-only Optimum Interpolation Sea Surface Temperature (OISST; Reynolds et al. 2007) which combines the AVHRR infrared observations and in situ data, available on 0.25° grid spacing from 1 September 1981 onward. To evaluate the atmospheric response to decadal variations of the KE system, we use ERA-Interim global atmospheric reanalysis produced by the European Centre for Medium-Range Weather Forecasts (ECMWF), with 0.75° horizontal grid spacing and 37 pressure levels from 1 January 1979 (Dee et al. 2011). Masunaga et al. (2015) have demonstrated that the increased resolution of SST prescribed for the ERA-Interim atmospheric model since January 2002 enables the representation of oceanic mesoscale (including fronts and eddies) imprints on MABL. Therefore, we use ERA-Interim 6-hourly and monthly data from 2002 to 2016 for analysis. Hereafter the average over 2002–16 is referred to as the long-term mean.

Based on the ERA-Interim 6-hourly data, the 3D total diabatic heating rate is estimated as the apparent heat source (Yanai and Tomita 1998), that is, a residual of the thermodynamic equation

$$Q = c_p \left(\frac{p}{p_0} \right)^\kappa \left(\frac{\partial \theta}{\partial t} + \mathbf{V}_h \cdot \nabla \theta + \omega \frac{\partial \theta}{\partial p} \right), \quad (1)$$

where $\mathbf{V}_h = (u, v)$ is the horizontal wind vector, ω is vertical velocity in pressure coordinates, θ is potential temperature, ∇ is the 2D gradient operator, $\kappa = R_d/c_p$ where R_d is the dry air gas constant and c_p the air specific heat capacity at constant pressure, and p is pressure with $p_0 = 1000$ hPa. The validity and reliability of this approach have been verified by Ling and Zhang (2013).

b. Statistical techniques

The time-lagged maximum covariance analysis (MCA) was first used in the pioneering work of Czaja and Frankignoul (2002) to study the impact of Atlantic SST anomalies on the North Atlantic Oscillation (NAO). Afterward, this powerful analysis tool has been widely used in the studies seeking for the climatic imprints of the midlatitude oceanic variability in the presence of internal atmospheric variability (e.g., Frankignoul and Kestenare 2005; Liu et al. 2006; Gan and Wu 2013, 2015; Wen et al. 2016; Zhang et al. 2018; Gan et al. 2019; L. Zhang et al. 2020). Here we use the time-lagged MCA to identify the distinctive change in the North Pacific atmospheric circulation in response to oceanic variability in the KE region. The time-lagged MCA performs a singular value decomposition (SVD) of the temporal covariance matrix of the normalized sea level pressure (SLP) and lagged SST anomaly fields to extract pairs of the leading covariant patterns that explain as much as possible of the mean squared covariance between SLP and SST. The expansion coefficients of SLP (SST) are derived by projecting the SLP (SST) anomaly field onto the left (right) singular vector derived from SVD. The statistical significance of the MCA statistics is assessed

by the Monte Carlo test. That is, each MCA at a specific time lag was repeated 1000 times using the original SST anomalies and the temporarily random permutation of SLP anomalies. The probability distribution of the randomized statistics was constructed to rank the significance level of the value being tested.

Monthly anomalies are obtained by subtracting the long-term monthly means and the linear long-term trend. A fourth-order Butterworth high-pass filter with cutoff of 6 days is used for construction of variables related to synoptic-scale eddies. The results based on the 2–8-day bandpass filter are qualitatively the same. To suppress atmospheric teleconnection from the tropics that could otherwise alias into the midlatitude response, a bivariate regression onto the two leading principal components of the tropical Pacific SST variations is applied and removed from all atmospheric anomaly fields prior to the time-lagged MCA and detailed analysis. The variance of areal-mean SLP anomalies of the midlatitude North Pacific is 42.8% lower after such ENSO-removal procedure. Meanwhile, the variance decreases of storm-track activity are merely within 10%.

3. Identification of oceanic forcing and atmospheric response

The midlatitude atmospheric response to frontal and mesoscale SST anomalies experiences significant subseasonal evolution (Taguchi et al. 2012; H. Seo et al. 2014; Révelard et al. 2016; Kuwano-Yoshida and Minobe 2017; Okajima et al. 2018; Czaja et al. 2019; Zhang et al. 2021). For this reason, we applied the time-lagged MCA to SLP anomalies fixed in a certain calendar month from October to April with SST anomalies leading or lagging by 0–3 months, with the analysis domain setting to the North Pacific basin (30°–55°N, 140°E–120°W) for SLP and the broad KE region (30°–45°N, 140°–175°E) for SST. Similar results are obtained by excluding the subarctic SST front region (38°–45°N) or setting both SLP and SST domains to the broad KE region. Figures 1a and 1b summarize the squared covariances and the correlation coefficients between the corresponding expansion coefficients of the first MCA modes, both of which measure how strongly the two fields are related to each other.

As can be seen, for the SST leading cases that imply the oceanic forcing of atmosphere, the squared covariance is of unique significance at the 90% confidence level at lag -2 when SLP is fixed in January, with the corresponding squared covariance fraction of 59%. There is a difference in distributions between the correlation coefficients and the squared covariances, with the large values mainly limited to February SLP for the former but January SLP for the latter, for reasons yet to be known. In MCA, however, higher spatial degrees of freedom enable easier construction of linear combinations that are highly correlated in the time domain (Wallace et al. 1992). Even when SLP is temporarily random permuted in the Monte Carlo test, most values of correlation coefficients are around 0.8–0.9, with less frequent smaller or larger values. Thus, the high correlation coefficient itself does not guarantee

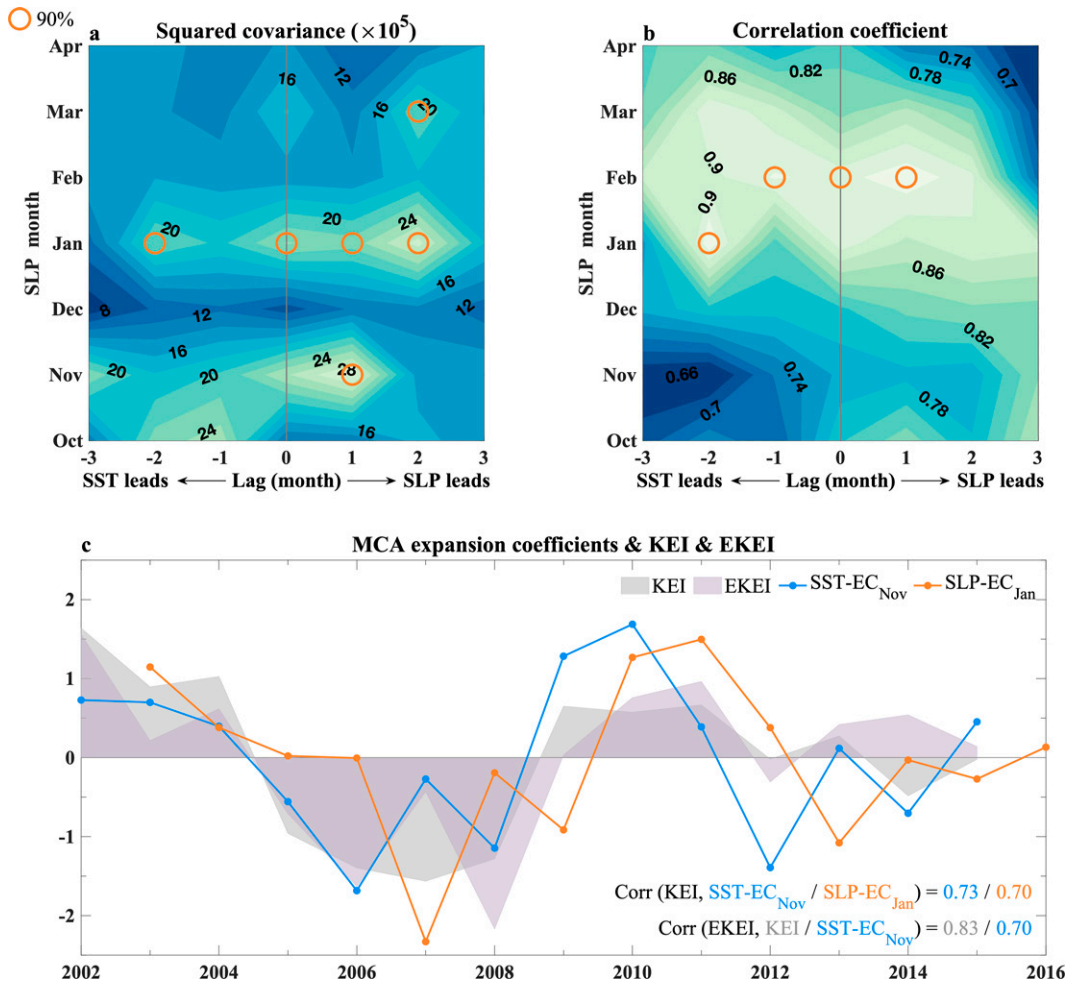


FIG. 1. (a) Squared covariances ($\times 10^5$; dimensionless) of the first MCA modes associated with the monthly anomalies of SST (30° – 45° N, 140° – 175° E) and SLP (30° – 55° N, 140° E– 120° W), and (b) correlation coefficients between their corresponding expansion coefficients. The ordinate denotes calendar months of SLP, and the abscissa denotes time lag of SST in month (positive when SST lags SLP). Values significant at the 90% confidence level based on the Monte Carlo test are marked with orange circles. (c) The normalized SST-EC_{Nov} (cyan), SLP-EC_{Jan} (orange), the winter-season-mean (from October to March) KEI (gray shading), and the November EKEI (purple shading; see text for definition).

significance and physical meaning. Nevertheless, the correlation between the SST expansion coefficients in November (hereafter SST-EC_{Nov}; cyan curve in Fig. 1c) and the SLP expansion coefficients in January (hereafter SLP-EC_{Jan}; orange curve in Fig. 1c) reaches the maximum of 0.94, consistent with the squared covariance performance. Therefore, the time-lagged MCA results suggest that SST anomalies confined to the KE region in November are associated with distinctive change in the North Pacific atmospheric circulation in the following January. Note that the areal-mean anomalies of KE SST in November exhibit high persistence to January while those of the wintertime northeastern Pacific SLP are barely persistent (not shown), supporting that the identified 2-month lag here reflects the SST anomalies persistence rather than the occurrence of SST forcing in advance.

The temporal evolution of SST-EC_{Nov} features decadal variations, which are synchronized to the wintertime KE variability at decadal time scales represented by the winter-season-mean (October–March) KE index (KEI; gray shading in Fig. 1c). The KEI is defined by Qiu et al. (2014) as the areal average of SSH anomaly in the KE southern recirculation gyre region (31° – 36° N, 140° – 165° E), with the positive (negative) value denoting the stable (unstable) dynamic state of the KE system. Here the KEI is significantly correlated with SST-EC_{Nov} and SLP-EC_{Jan} ($r = 0.73$ and 0.70), indicating a close link between the KE dynamic state variations and the air–sea coupling mode extracted by MCA. Given the well-established upstream and downstream eddy kinetic energy (EKE) seesaw associated with the decadal KE variations (Qiu et al. 2017; Yang et al. 2018), we constructed an EKE index (EKEI) to further verify the

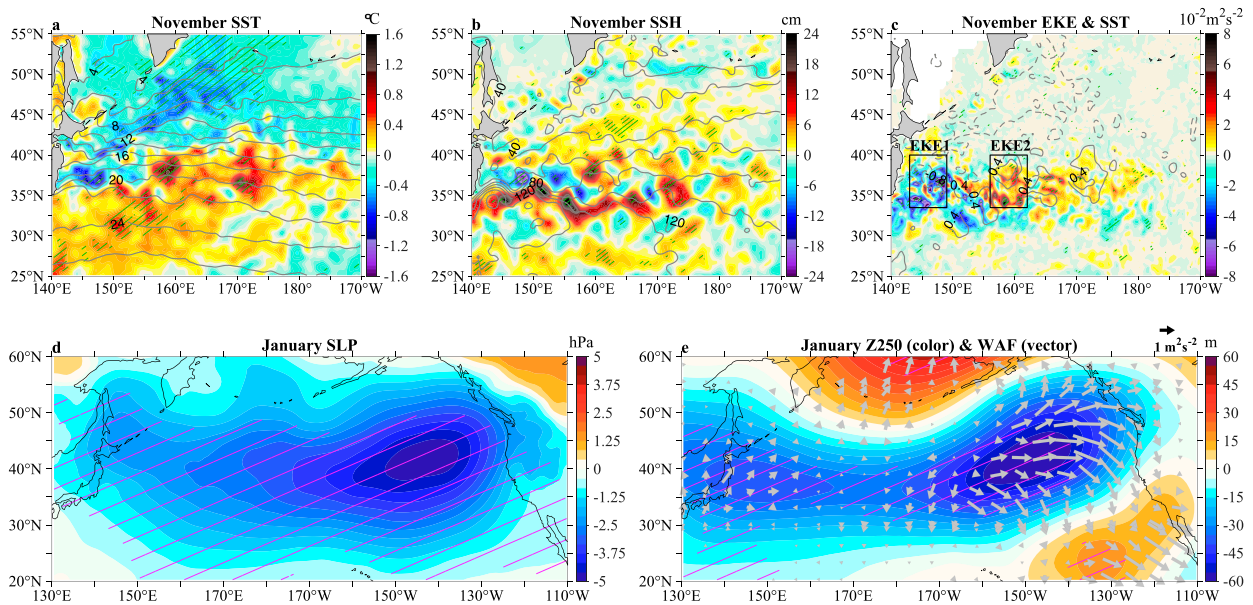


FIG. 2. Regressions (colors) of (a) SST ($^{\circ}\text{C}$), (b) SSH (cm), and (c) EKE ($10^{-2} \text{ m}^2 \text{ s}^{-2}$) in November, and of (d) SLP (hPa) and (e) Z250 (m) in January. Regressions are computed with monthly anomalies against SST-EC_{Nov}. Contours in (a) and (b) denote the November long-term mean. Contours in (c) denote regressions of SST [repeat of (a) colors]. Boxes in (c) denote the two areas for calculating EKEI (i.e., purple shading in Fig. 1c). Arrows in (e) denote January wave activity flux ($\text{m}^2 \text{ s}^{-2}$) associated with SST-EC_{Nov}. Hatching indicates regression significant at the 90% confidence level.

connection between SST-EC_{Nov} and the decadal state change in the KE system. Here EKE is calculated with 300-day high-passed oceanic surface geostrophic velocity derived from SSH. The EKEI (purple shading in Fig. 1c) is computed as differences of areal mean EKE in the downstream ($156^{\circ}\text{--}162^{\circ}\text{E}$, $33.5^{\circ}\text{--}40^{\circ}\text{N}$; right box in Fig. 2c) and upstream ($143^{\circ}\text{--}149^{\circ}\text{E}$, $33.5^{\circ}\text{--}40^{\circ}\text{N}$; left box in Fig. 2c) areas, which are found to be significantly correlated with winter-time KEI ($r = 0.83$) and SST-EC_{Nov} ($r = 0.70$).

Overall, the above results support that SST-EC_{Nov} reflects the decadal KE variations and exploration of the air–sea coupling processes associated with SST-EC_{Nov} is helpful in understanding the decadal variations of the KE system from the point of view of ocean–atmosphere interaction. In the following analysis, we adopt the linear regression against SST-EC_{Nov} to illustrate the atmospheric responses and the dynamical processes involved in the following January. The 2-month lagged regression rather than simultaneous regression prevents the contamination of atmospheric response by concurrent atmospheric forcing signal. The number of effective degrees of freedom for regression is $N_{\text{EC}} - 2$, where $N_{\text{EC}} = 10.43$ is the effective sample size of SST-EC_{Nov}. It is estimated as dividing the length of SST-EC_{Nov} by its effective decorrelation time, which is computed based on Metz [1991, their Eqs. (A1) and (A3)] with autocorrelations of five time lags being used.

Figures 2a–c show the anomalous SST, SSH, and EKE patterns associated with SST-EC_{Nov}. Collectively, the KE system exhibits a strengthened and less convoluted jet, subdued (vigorous) mesoscale eddy activity in the upstream

(downstream), and prevalent downstream mesoscale warm SST anomalies. These oceanic forcing patterns are in line with the stable KE path state. Specifically, the ringed warm SST anomalies are accompanied with high EKE in the vicinity and are collocated with positive SSH anomalies, with the strongest ones existing in the downstream transition region between the Subarctic Front and the KE jet (hereafter the KE transition region). A snapshot analysis supports the attribution of downstream SST warming to active downstream mesoscale motions associated with stable KE path state (not shown). In the KE transition region, the association of warm SST anomalies with anticyclonic eddies has been well documented (e.g., Sugimoto and Hanawa 2011; Kouketsu et al. 2012; Sasaki and Minobe 2015). Particularly, Sasaki and Minobe (2015) reported that a warm SST anomaly at $37^{\circ}\text{--}39^{\circ}\text{N}$, $157^{\circ}\text{--}161^{\circ}\text{E}$, as we observed here, occurs with enhanced downstream eddy activity. They suggested that the heat transport induced by the pinched-off eddies is substantial to the interannual-to-decadal SST variations in the KE region. Yang et al. (2018) further revealed that the enhanced downstream eddy activity results from the stabilized upstream KE jet via lateral advection. On the other hand, some studies reported that the downstream warm SST anomalies are also attributable to a northeastward flow bifurcating from the KE at around 150°E , during the KE stable period (Sugimoto 2014; Hosoda et al. 2015). Given that the power spectrum of the SST anomaly field observed here peaks at $\sim 300 \text{ km}$ (not shown), there may be additional contribution of the KE bifurcation to the SST warming in the downstream transition region. The above

evidence collectively indicates that oceanic mesoscale motions associated with the decadal KE variations induce pronounced downstream mesoscale SST warming, which further influences the atmospheric circulation as revealed next.

Figures 2d and 2e show the regression maps against SST-EC_{Nov} of SLP and geopotential height at 250 hPa (Z250) in January. Similar maps can be obtained by regressing against the November KEI or EKEI, either in the current analysis period of 2002–16 or in 1993–2019 (not shown). The atmospheric responses feature a basin-scale equivalent-barotropic structure, with a well-defined center of anomalous low pressure reaching 5 hPa and upper-level cyclonic anomaly reaching 60 m over the northeastern Pacific. In addition, the Z250 regression displays a moderate cyclonic anomaly centered over the KE transition region. Such pattern closely resembles the transient atmospheric response to warm SST anomalies in the KE transition region revealed by Wills and Thompson (2018). Accompanying with the basin-scale cyclonic anomaly, two anticyclonic anomalies can be seen over the Chukchi–Bering Sea and the eastern subtropical North Pacific.

To understand how those anomalous Z250 lobes are connected, we diagnose the energy propagation of stationary Rossby wave packets using wave activity flux (WAF) proposed by Takaya and Nakamura (2001). This flux is parallel to the local group velocity relative to the zonally varying background flow. Its divergence (convergence) signifies where the wave packet is emitted (absorbed), indicating the source (sink) of wave activity. The horizontal WAF is calculated as

$$\text{WAF} = \frac{P}{2|U|} \left[U(\psi_x^{*2} - \psi^* \psi_{xx}^*) + V(\psi_x^* \psi_y^* - \psi^* \psi_{xy}^*) \right. \\ \left. + U(\psi_y^* \psi_x^* - \psi^* \psi_{yx}^*) + V(\psi_y^{*2} - \psi^* \psi_{yy}^*) \right], \quad (2)$$

where ψ^* is the geostrophic streamfunction perturbation associated with SST-EC_{Nov}, $U = (U, V)$ is the long-term mean wind velocity, and P is pressure scaled by 1000 hPa.

As shown in Fig. 2d (arrows), the WAF converging poleward into the anticyclonic anomaly over the Chukchi–Bering Sea primarily emanates from the KE region, indicating that the SST-forced upper-level divergences over the KE region could generate Rossby wave source. Another source is found over the northeastern Pacific where the WAF propagates southeastward to the anticyclonic anomaly therein. We note that there is no significant connection of WAF between the KE region and the northeastern Pacific, suggesting that stationary Rossby waves have little role to play in linking the cyclonic anomaly over those two regions. The synoptic-eddy-mediated processes could be a bridge linking the upstream and downstream cyclonic responses, given that the equilibrium barotropic response of large-scale atmospheric circulation depends on the nature of feedback of transient eddies migrating along storm tracks (e.g., Kushnir et al. 2002; Peng et al. 2003; Deser et al. 2007; Taguchi et al. 2012; Fang and Yang 2016; Okajima et al. 2018; Xue et al. 2018). This point will be explored in the next section.

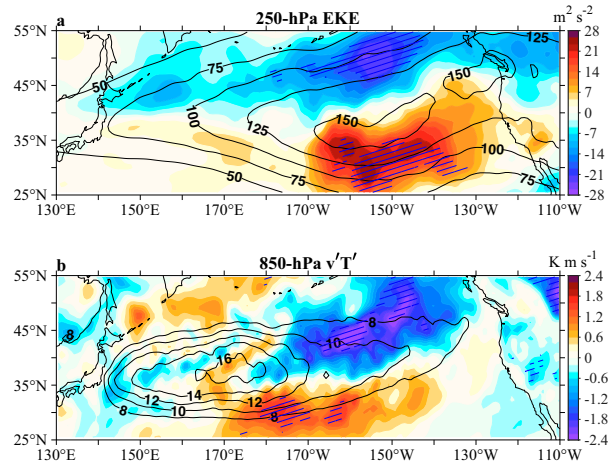


FIG. 3. Regressions (colors) onto SST-EC_{Nov} of (a) 250-hPa synoptic EKE ($\text{m}^2 \text{s}^{-2}$) and (b) 850-hPa poleward synoptic eddy heat flux $\overline{v'T'}$ (K m s^{-1}) in January, overlaid with their January long-term mean (black contours). Hatching indicates regression significant at the 90% confidence level.

4. Mechanism of atmospheric response

a. Storm-track response and its feedback on basin-scale time-mean flow

How does the storm-track activity change and thereby link the basin-scale anomalous low to thermal forcing of the KE system? Here the upper- and lower-level storm-track activity is represented by the synoptic EKE at 250 hPa and the poleward synoptic eddy heat flux ($\overline{v'T'}$) at 850 hPa, respectively. Figure 3 shows the regression maps against SST-EC_{Nov} of the 250-hPa EKE and the 850-hPa $\overline{v'T'}$ in January. The EKE response pattern (Fig. 3a) displays a well-defined meridional dipole structure over the downstream basin, with the north-negative and south-positive lobes straddling its axis of long-term-mean maximum and reaching the west coast of North America. The EKE anomaly dipole is also discernible over the upstream basin, albeit that its amplitude is much weaker and not statistically significant. In response to the dominant warm SST anomalies in the KE region, the $\overline{v'T'}$ shows weak negative anomalies locally, whereas to east of 170°E the meridional dipole response is clearly visible. Collectively, the results reflect the southward deflection of storm tracks, which is presumed to regulate basin-scale time-mean flow via the transient eddy feedback forcing from anomalous eddy heat and vorticity fluxes.

To quantify the net eddy feedback, we evaluate the eddy-induced geopotential height tendency as in Lau and Holopainen (1984), Nishii et al. (2009), and Fang and Yang (2016):

$$\left(\frac{\partial \bar{Z}}{\partial t} \right)_{\text{eddy}} = \left[\nabla^2 + f^2 \frac{\partial}{\partial p} \left(\frac{1}{\sigma} \frac{\partial}{\partial p} \right) \right]^{-1} \\ \times \left\{ -\frac{f}{g} \nabla \cdot \overline{\mathbf{V}_h' \zeta'} + \frac{f^2}{g} \frac{\partial}{\partial p} \left[\frac{\nabla \cdot \overline{\mathbf{V}_h' \theta'}}{-(\partial \Theta / \partial p)} \right] \right\}, \quad (3)$$

Z tendency (color) induced by eddy heat and vorticity fluxes & EFS (contour)

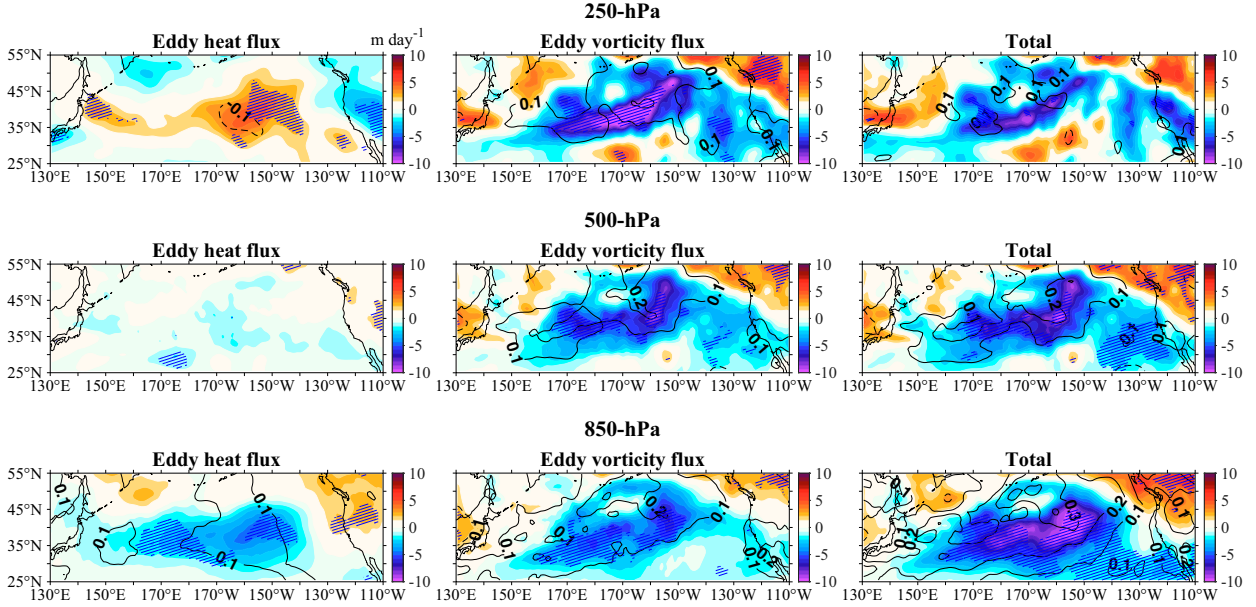


FIG. 4. Regressions (colors) onto SST-EC_{Nov} of Z_{tend} (m day^{-1}) induced by the convergence of (left) transient eddy heat flux, (center) eddy vorticity flux, and (right) the sum of these two fluxes at (top) 250, (middle) 500, and (bottom) 850 hPa in January, overlaid with their associated EFS (black contours). Hatching indicates regression of Z_{tend} is significant at the 90% confidence level.

where $\sigma = -\alpha\Theta^{-1}(\partial\Theta/\partial p)$ is the background static stability parameter with α the specific volume, ζ is the relative vorticity, Θ is the potential temperature of the background state (global zonal mean), and other notations conform to previous definitions; primes denote synoptic fluctuations and overbars denote monthly means. On the left-hand side (lhs) of (3), $\partial\bar{Z}/\partial t$ signifies the monthly-mean geopotential height tendency (Z_{tend}) induced by the convergence of transient eddy vorticity and heat fluxes represented by the first and second terms in the brace on the right-hand side (rhs), respectively. To approximate the local efficiency of transient eddy feedback in replenishing the stationary circulation anomalies, we quantify the amount of eddy-induced Z_{tend} per unit geopotential height change, referred to as the eddy feedback strength (EFS) introduced by Choi et al. (2010):

$$\text{EFS} = \frac{\int Z_a E_a dt}{\int Z_a^2 dt}, \quad (4)$$

where dt is monthly interval, and Z_a and E_a denote the geopotential height anomaly and eddy-induced $\partial\bar{Z}/\partial t$ anomaly in (3), respectively. Here EFS is computed for January at each grid point. Positive (negative) EFS represents transient eddies acting to reinforce (impair) the anomalous low-frequency flow, with higher value signifying stronger efficacy of eddy feedback.

Figure 4 shows the anomalous eddy-induced Z_{tend} in January regressed upon SST-EC_{Nov} and the corresponding EFS. The Z_{tend} due to anomalous eddy thermal forcing (left column) depicts a basin-scale baroclinic response with

the anticyclonic (cyclonic) anomaly at 250 hPa (850 hPa), whereas a distinct barotropic response with the cyclonic anomalies throughout the troposphere is evident for the Z_{tend} due to anomalous eddy vorticity forcing (middle column). In total (right column), the anomalous transient eddy activity exerts net positive feedback that reinforces the barotropic cyclonic circulation anomaly in response to the decadal SST-EC_{Nov} evolution (i.e., the decadal dynamic state change in the KE system). More specifically, the total tendency field shows prominent negative anomalies extending from the downstream KE transition region to the northeastern basin, illustrating the maximum convergence of anomalous eddy heat and vorticity fluxes resulting from the southward deflection of storm tracks. From the EFS perspective, the positive EFS is strongest in the lower troposphere, with the maximum above the downstream KE transition region, and generally decreases with height. The basin-average EFS at 250 hPa is 0.035 day^{-1} , indicating that the anomalous eddy feedback forcing may take ~ 28 days to replenish the stationary cyclonic anomalies. In contrast, the positive eddy feedback at 850 hPa could be so efficient that the replenishing time scale is ~ 6 days (0.182 day^{-1} EFS). This rough estimate is, to some extent, consistent with Okajima et al. (2018).

Further column-integrated energetics analysis shows that the baroclinic available potential energy conversion from the climatological-mean state and the barotropic kinetic energy gain via both synoptic-eddy nonlinear feedback and background mean flow are important energy sources of the cyclonic circulation response pattern for its maintenance (see

appendix A for details). In general, it is reasonable to speculate that the southward-deflected synoptic eddies have efficacy in fostering the basin-scale equivalent-barotropic cyclonic anomaly, which is further maintained by energy conversion from the background state.

b. Synoptic eddy temperature variance budget

Why do storm tracks deflect southward? Since synoptic eddies feed off eddy available potential energy (EAPE), we now consider changes in the synoptic eddy temperature variance (T'^2), which is proportional to EAPE and the associated energy conversion. Figure 5a shows the distribution of T'^2 response at 550 hPa, the level at which the long-term-mean T'^2 maximum occurs. It is evident that T'^2 is significantly southward deflected, manifesting as positive anomalies along the KE latitudinal band and negative anomalies spreading over the northeastern basin. In particular, significant positive T'^2 over the KE region is collocated with the substantially enhanced convective precipitation (Fig. 5b), reflecting the imprints of enhanced storm activity carrying abundant moisture. Looking closer over the KE region, finer-scale enhancement of convective precipitation is confined to above 155°–160°E and 170°–175°E at around 37°N where the ringed warm SST anomaly locates (cf. Fig. 2a), hinting at potential influence of warm eddies in the downstream transition region. As for the large-scale precipitation, its response over the eastern basin is due to the anomalous cyclonic circulation, which brings warm moist air northeastward and cold dry air southwestward (arrows in Fig. 5c). The increased rainfall over California during the KE stable period has been reported previously (X. Ma et al. 2015; Siqueira et al. 2021), to which the enhanced large-scale precipitation is the main contributor. On the other hand, the weakened large-scale precipitation over the KE region counteracts the enhanced convective one, acting to obscure the imprint of SST variability on total precipitation, as pointed out by Masunaga et al. (2016).

Next, the synoptic eddy temperature variance (T'^2) budget (see appendix B for derivation) regarded as a proxy for EAPE budget is analyzed:

$$0 = \underbrace{-\nabla'_h T' \cdot \nabla \bar{T}}_{\text{Baroclinic conversion}} + \underbrace{\omega' T' S_p}_{\text{EKE conversion}} + \underbrace{\frac{1}{c_p} \bar{Q}' T'}_{\text{Diabatic source}} - \underbrace{\frac{1}{2} \nabla \cdot \nabla'_h T'^2}_{\text{Horizontal transport}} - \underbrace{\left(\frac{\partial}{\partial p} - \frac{\kappa}{p} \right) \omega' T'^2}_{\text{Vertical transport}} + \text{Res}, \quad (5)$$

where $\bar{S}_p = [R_d \bar{T} / (c_p p)] - (\partial \bar{T} / \partial p)$ is the static stability and \bar{Q} the total diabatic heating rate; primes denote synoptic fluctuations and overbars denote monthly means; other notations conform to previous definitions. The residual term Res contains the tendency term and terms related to nonsynoptic fluctuations. Contours in Fig. 6 depict the long-term-mean distribution of each term on the rhs of (5) at 550 hPa. Climatologically, the major source of EAPE is baroclinic conversion from the mean

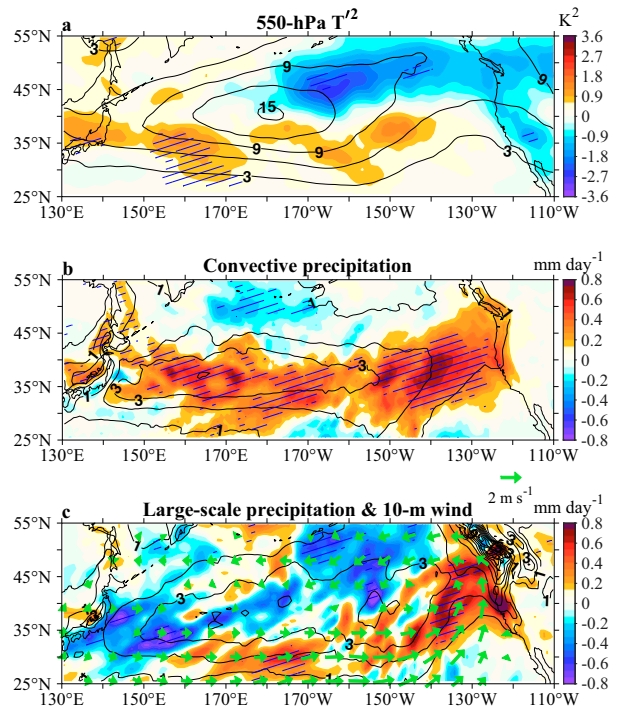


FIG. 5. Regressions (colors) onto SST-EC_{Nov} of (a) 550-hPa T'^2 (K^2), (b) convective precipitation (mm day^{-1}), and (c) large-scale precipitation (mm day^{-1}) and 10-m wind (arrows; m s^{-1}) in January, overlaid with their January long-term mean (black contours). Hatching indicates regression is significant at the 90% confidence level.

flow available potential energy (the first term). Diabatic processes such as latent heat release also play an indispensable role in supplying EAPE especially in the downstream region (the third term). The generation of EAPE is largely balanced by conversion to EKE (the second term) and is redistributed primarily by horizontal transport (the fourth term). Both vertical redistribution and residual (the last two terms) are small compared with other terms. The above interpretation of the T'^2 budget confirms Chang et al. (2002). From the total energetics point of view, they concluded that transient eddies gain energy via baroclinic conversion and, to a lesser extent, diabatic conversion, and highlighted that much of energy is transferred to neighboring eddies downstream via the ageostrophic geopotential fluxes. This so-called downstream development process is intrinsic to the coherent baroclinic wave packets consisting of synoptic eddies.

Color shadings in Fig. 6 depict the 550-hPa regression of each of the above-mentioned term against SST-EC_{Nov}. As can be seen, baroclinic conversion shows a clear southward displacement in agreement with the storm-track response (Fig. 6a). A similar shift is discernible in the diabatic sources, with positive anomalies dominant east of 170°E (Fig. 6c). This downstream increased EAPE generation by diabatic conversion is conducive to the southward

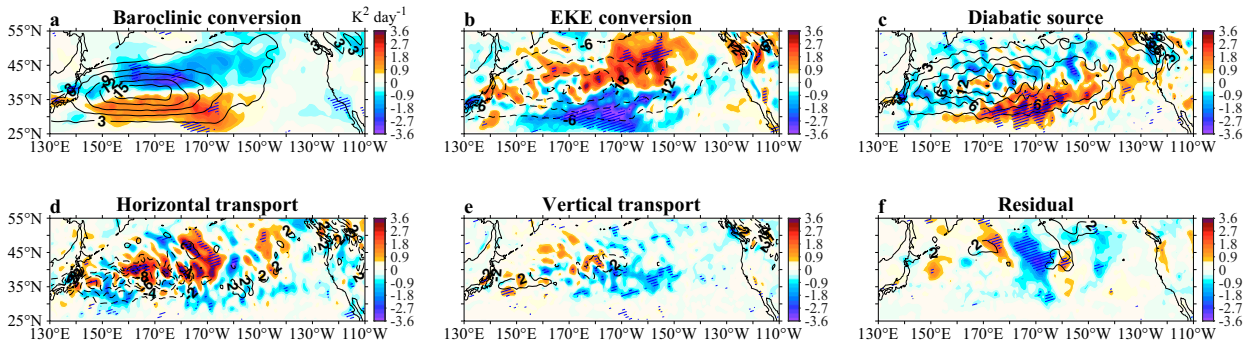
550-hPa T'^2 budget

FIG. 6. (a)–(f) Regressions (colors) onto SST-EC_{Nov} of 550-hPa $\overline{T'^2}$ budget terms [see (5) for details; $\text{K}^2 \text{ day}^{-1}$] in January, overlaid with their January long-term mean (black contours). Hatching indicates regression is significant at the 90% confidence level.

and downstream extension of storm-track activity that stems from the shifted baroclinic conversion. Changes in those two EAPE sources are largely balanced by conversion to EKE (Fig. 6b) and partially by horizontal transport (Fig. 6d). Responses of vertical transport and residual are relatively weak (Figs. 6e,f). The southward displacement of the conversion from EAPE to EKE helps to shape the corresponding change in the 550-hPa EKE (not shown), given the similarity of both fields and its leading role in the EKE budget (e.g., Takahashi and Shirooka 2014). It is notable

that the disorganized distribution of the anomalous EKE conversion over the western basin seems to correspond to the anomalous diabatic source field, indicating a close relationship between deep-reaching vertical motion and diabatic heating. We will return to this point later.

Focusing on the storm-track entrance region, we further analyze the latitudinal–vertical section of the 155°–165°E zonal-mean response of the $\overline{T'^2}$ budget terms. This averaging section is chosen based on the location where the prominent warm SST anomaly and positive $\overline{T'^2}$ center locates

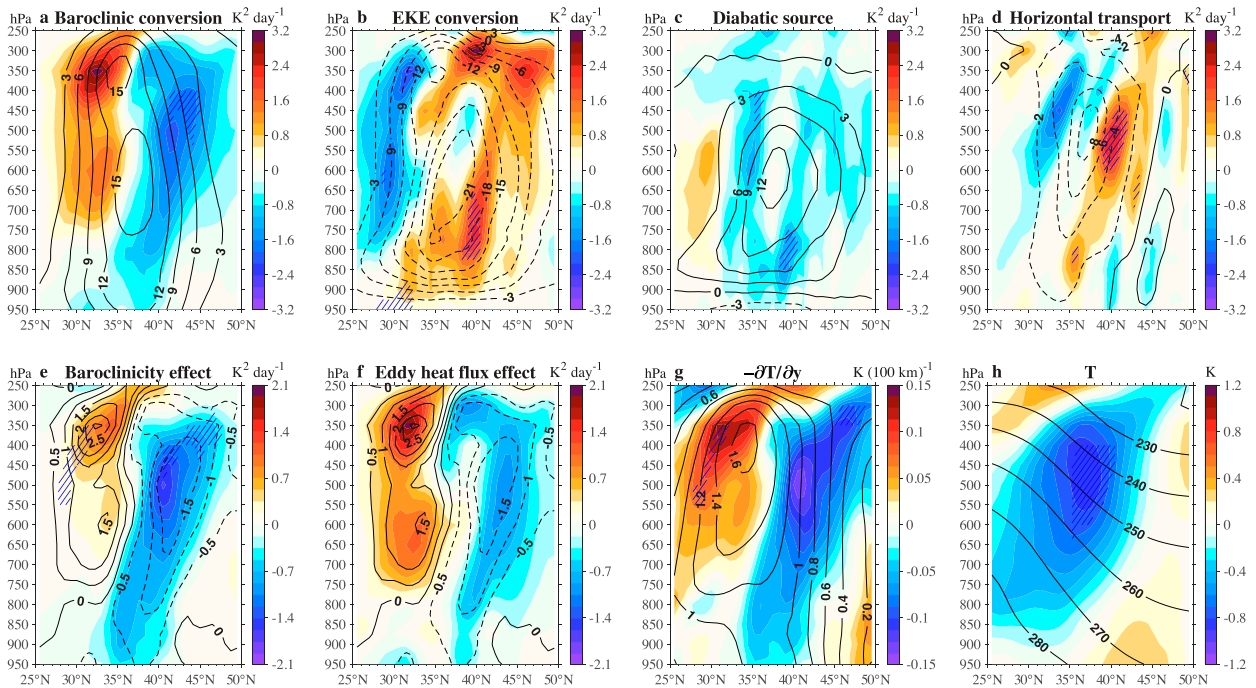


FIG. 7. Latitude–pressure sections of 155°–165°E zonal-mean regressions (colors) of (a)–(d) $\overline{T'^2}$ budget terms (as in Figs. 6a–d; $\text{K}^2 \text{ day}^{-1}$), and of $\overline{T'^2}$ baroclinic conversion ($\text{K}^2 \text{ day}^{-1}$) induced by (e) baroclinicity change and (f) transient eddy heat flux change separately, and of (g) meridional temperature gradient ($\text{K per } 100 \text{ km}$) and (h) temperature (K). Black contours denote the January long-term mean except in (e) and (f), where they indicate regressions of total baroclinic conversion [repeats of (a) colors]. Regressions are computed with monthly anomalies in January against SST-EC_{Nov}. Hatching indicates regression is significant at the 90% confidence level.

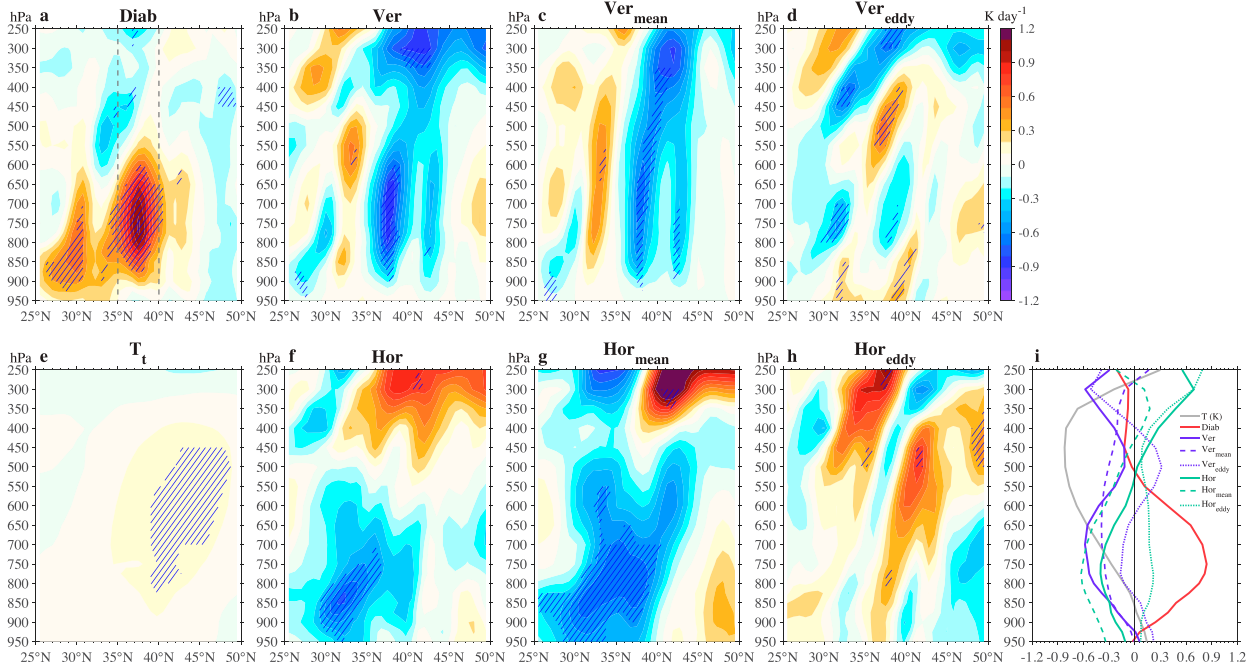


FIG. 8. (a)–(h) Latitude–pressure sections of 155°–165°E zonal-mean regressions (colors) of thermodynamic budget terms [see Eq. (7) for detail; K day^{-1}]. (i) Vertical profiles of 35°–40°N, 155°–165°E areal-mean regressions of temperature (K) and thermodynamic budget terms [i.e., meridional means of (a)–(d) and (f)–(h) bounded by the dashed black lines in (a)]. Regressions are computed with monthly anomalies in January against SST-EC_{Nov}. Hatching indicates regression is significant at the 90% confidence level.

(cf. Figs. 2a and 5a). Similar results are obtained by taking zonal average of 155°–175°E. It is evident that baroclinic conversion is the main driver of the southward-displaced EAPE generation, characterized as large negative (positive) anomalies tilting poleward with height on the northern (southern) flank of its long-term-mean core over the KE transition region (35°–45°N) (Fig. 7a). Correspondingly, both the EAPE-to-EKE conversion (Fig. 7b) and the horizontal EAPE transport (Fig. 7d) are suppressed at higher latitudes but more active to the south, relative to their long-term mean. The diabatic source is overall decreased but its anomaly amplitude is much weaker than the baroclinic conversion (Fig. 7c). Looking closer, the anomalous baroclinic conversion and diabatic source offsets each other at midlevels (650–450 hPa) around 35°N and thereby leading to a trivial change in EKE conversion. But the opposite case holds for the low-level response of EKE conversion around 40°N. Changes in the other two terms are messy and fairly weak (not shown).

Change in baroclinic conversion can be due to the direct effect of mean baroclinicity and the indirect effect of transient eddy heat flux (Foussard et al. 2019). To separate these two effects, we decompose the baroclinic conversion anomaly as follows:

$$-[\overline{\mathbf{V}_h' T'} \cdot \nabla \overline{T}]_a = -[\overline{\mathbf{V}_h' T'}]_c \cdot [\nabla \overline{T}]_a - [\overline{\mathbf{V}_h' T'}]_a \cdot [\nabla \overline{T}]_c + \text{Res}, \quad (6)$$

where $[\]_c$ signifies the long-term monthly mean and $[\]_a$ signifies the monthly deviation therefrom, and Res contains other terms of smaller magnitude. The first and second terms

on the rhs of (6) respectively represent the anomalous baroclinic conversion solely induced by the anomalous lateral temperature gradient (i.e., baroclinicity) and the anomalous transient eddy heat flux. As shown in Figs. 7e and 7f, the baroclinicity-induced negative conversion anomalies on the northern flank around 40°N have larger amplitude than that induced by the eddy heat flux and match well with the total baroclinic conversion distribution. On the southern flank, the eddy-induced positive anomalies seem to take the lead. It is speculated that the southward displacement of baroclinicity primarily drives the shifted EAPE source, which is further fostered by the subsequent shift of eddy heat flux. Further analysis shows that the displaced baroclinicity is due to the displaced meridional temperature gradient (Fig. 7g), which is ultimately caused by the anomalously cold temperature over the KE transition region with the maximum cooling at midlevels (Fig. 7h). Such midlevel cooling is crucial for the southward migration of storm-track activity and hence essential in the generation and maintenance of the equivalent-barotropic cyclonic response.

c. Thermodynamic response

What physical processes are responsible for the midlevel cooling? The thermodynamic budget in the KE region is performed to address this issue:

$$0 = \underbrace{-\frac{\partial \overline{T}}{\partial t}}_{T_t} - \underbrace{\overline{\mathbf{V}_h} \cdot \nabla \overline{T}}_{\text{Hor}} - \underbrace{\left(\overline{\omega \frac{\partial T}{\partial p}} - \frac{\kappa}{p} \overline{\omega T} \right)}_{\text{Ver}} + \underbrace{\frac{1}{c_p} \overline{Q}}_{\text{Diab}}, \quad (7a)$$

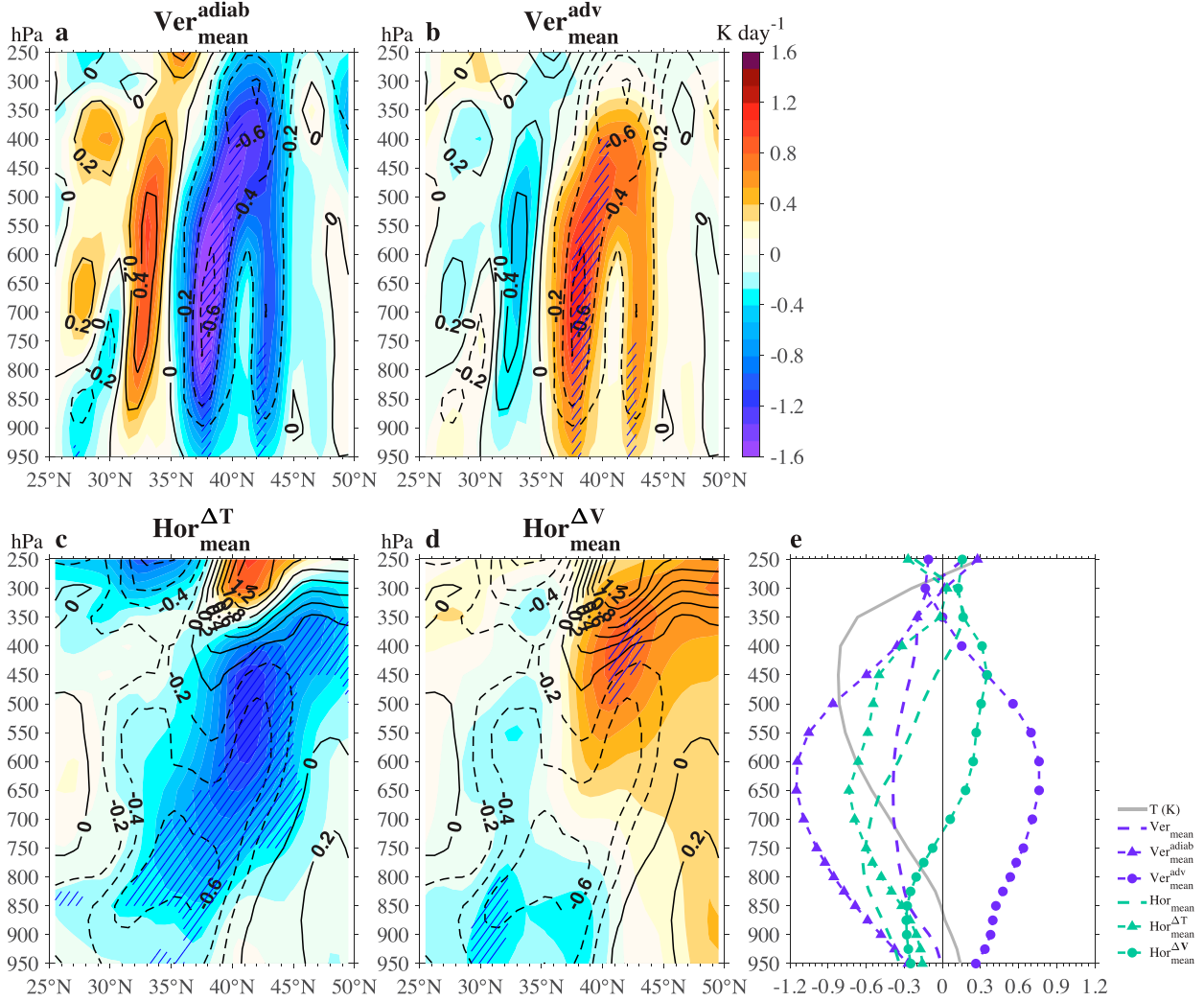


FIG. 9. Latitude–pressure sections of 155°–165°E zonal-mean regressions (colors) of (a) Ver_{mean}^{adiab} , (b) Ver_{mean}^{adv} , (c) $Hor_{mean}^{\Delta T}$, and (d) $Hor_{mean}^{\Delta V}$, overlaid with regressions (black contours) of Ver_{mean} in (a) and (b) and Hor_{mean} in (c) and (d) [see Eq. (8) for details; $K day^{-1}$]. (e) As in Fig. 8i but for temperature (K) and budget terms shown in (a)–(d). Regressions are computed with monthly anomalies in January against SST-EC_{Nov}. Hatching indicates regression is significant at the 90% confidence level.

where notations conform to previous definitions. On the rhs of (7a), the term “Tt” is the temperature tendency, the term “Hor” is the horizontal advection of temperature, the two parts in term “Ver” respectively represent the vertical advection and the adiabatic expansion, and the term “Diab” is the rate of temperature change induced by total diabatic heating. We further break down Hor and Ver into mean and eddy components as follows:

$$Hor = \underbrace{-\bar{V}_h \cdot \nabla \bar{T}}_{Hor_{mean}} - \underbrace{\nabla \cdot \bar{V}_h' T'}_{Hor_{eddy}} + \overline{T' \nabla \cdot V_h'}, \quad (7b)$$

$$Ver = \underbrace{-\left(\bar{\omega} \frac{\partial \bar{T}}{\partial p} - \frac{\kappa}{p} \bar{\omega} \bar{T}\right)}_{Ver_{mean}} - \underbrace{\left(\frac{\partial}{\partial p} - \frac{\kappa}{p}\right) \bar{\omega}' T'}_{Ver_{eddy}} + \overline{T' \frac{\partial \omega'}{\partial p}}, \quad (7c)$$

where prime denotes the deviation from the monthly mean. The last term on the rhs of (7b) and (7c) is one to two orders of magnitude smaller than the other two terms and thus is negligible.

Figure 8 depicts responses of the thermodynamic budget terms in (7a)–(7c). The main balances found in the total thermodynamic budget [(7a)] are the following: 1) strong lower-to-midlevel diabatic heating (Fig. 8a), confined to the KE transition region where both markedly warm SST anomalies and enhanced convective precipitation exist, balanced by anomalous cooling induced by vertical transport and horizontal advection (Figs. 8b,f); 2) less intense diabatic heating at lower latitudes balanced by cold horizontal advection; and 3) compensating cold vertical transport with warm horizontal advection at upper levels. The local anomalous temperature tendency is negligible throughout the troposphere

(Fig. 8e). Distributions of mean and eddy components further show that the strong confined diabatic heating at 900–600 hPa (Fig. 8i, red line) is mainly balanced by a lower-to-midlevel cold horizontal advection by the mean flow (Figs. 8g,i, green dashed line), a deep-reaching cooling due to the mean vertical transport throughout the troposphere (Figs. 8c,i, purple dashed line), and, to a lesser extent, the vertical eddy component (Figs. 8d,i, purple dotted line). The mean component of horizontal advection balances the relatively weak diabatic warming at lower latitudes. Particularly for 550–400 hPa where the strongest midlevel cooling exists (Fig. 8i, gray line), the mean vertical transport induced cooling is the dominant term. Above 350 hPa, the mean/eddy components of horizontal and vertical transport mainly compensate each other. The upper-level southward warming induced by the eddy lateral advection (Fig. 8h) is consistent with the southward migration of storm tracks.

As revealed by the results above, the midlevel cooling that drives the southward deflection of storm-track activity and subsequent large-scale atmospheric responses is attributable to both the mean components of anomalous vertical and horizontal transport. We further split the mean vertical and horizontal transport terms to distinguish the different processes involved in the generation of the anomalous cooling. The mean vertical transport (Ver_{mean}) consists of the mean vertical temperature advection $[-\bar{\omega}(\partial\bar{T}/\partial p)]$ and the adiabatic expansion $[(\kappa/p)\bar{\omega}\bar{T}]$, referred to as $\text{Ver}_{\text{mean}}^{\text{adv}}$ and $\text{Ver}_{\text{mean}}^{\text{adiab}}$, respectively. For the mean horizontal advection, we adopt the same approach as (6):

$$-[\bar{\mathbf{V}}_h \cdot \nabla \bar{T}]_a = -[\bar{\mathbf{V}}_h]_c \cdot [\nabla \bar{T}]_a - [\bar{\mathbf{V}}_h]_a \cdot [\nabla \bar{T}]_c + \text{Res.} \quad (8)$$

The first and second terms on the rhs of (8) are referred to as $\text{Hor}_{\text{mean}}^{\Delta T}$ and $\text{Hor}_{\text{mean}}^{\Delta V}$, representing the advection of anomalous temperature by the background wind and the advection of background temperature by the anomalous wind, respectively.

As can be seen from Figs. 9a and 9b, responses of the adiabatic expansion and the vertical advection have similar patterns of opposite signs (color shadings), and the dominance of the former over the latter determines change in the mean vertical transport (contours). Particularly, the adiabatic warming and cooling confined within narrow bands coincide well with the anomalous descending and ascending motions, with the strongest updraft and cooling reaching deep into the upper troposphere over the KE transient region (cf. Fig. 11a). In addition, the anomalously cold lateral advection at midlevel comes from the advection of cold temperature anomalies by the background flow (Fig. 9c), whereas the advection of background temperature by the cyclonic circulation anomaly primarily contributes to the low-level cold advection south of the KE region (Fig. 9d). Collectively, the result points to the marked contribution to the midlevel cooling [Fig. 9e (gray line)] of the adiabatic cooling and the lateral advection solely due to cold temperature anomalies [Fig. 9e (dashed lines with triangle)].

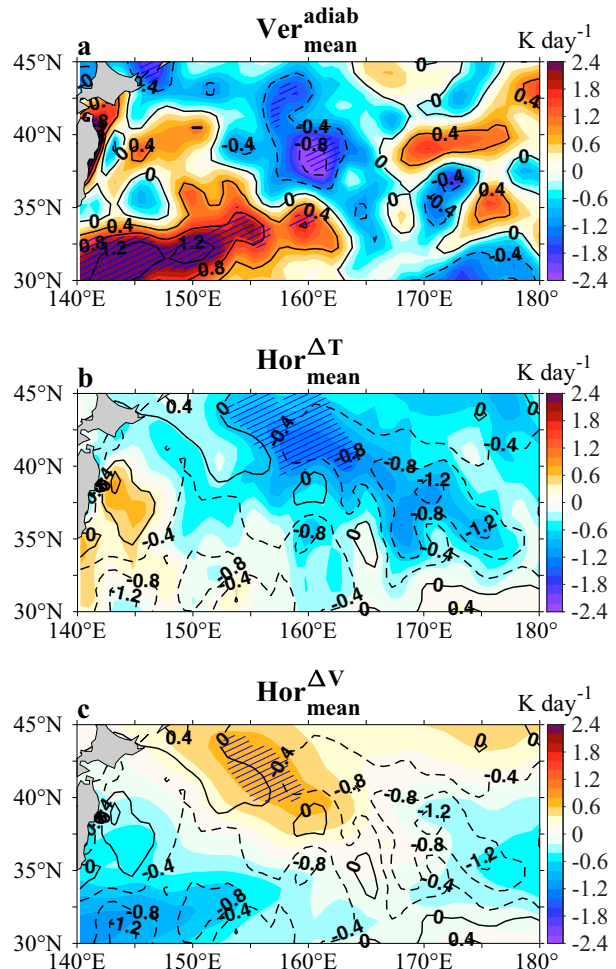


FIG. 10. Regressions onto SST-ECNov of (a) $\text{Ver}_{\text{mean}}^{\text{adiab}}$, (b) $\text{Hor}_{\text{mean}}^{\Delta T}$, and (c) $\text{Hor}_{\text{mean}}^{\Delta V}$ (colors) at 550 hPa in January, overlaid with regressions (black contours) of Ver_{mean} in (a) and Hor_{mean} in (b) and (c) [see Eq. (8) for detail; K day^{-1}]. Hatching indicates regression is significant at the 90% confidence level.

Now we take a close look at the spatial distributions of $\text{Ver}_{\text{mean}}^{\text{adiab}}$, $\text{Hor}_{\text{mean}}^{\Delta T}$, and $\text{Hor}_{\text{mean}}^{\Delta V}$ responses at 550 hPa. The advection of cold temperature anomalies generally locates to the east of the significant adiabatic cooling in the downstream KE transition region, with both being oriented from northwest to southeast (color shadings in Figs. 10a,b). It is suggested that such cold lateral advection stems from the advection of adiabatic cooling by the background prevailing northwesterly wind. Moreover, comparison of color shadings and contours in Figs. 10b and 10c demonstrates that distinct cold lateral advection comes from the advection of cold temperature anomalies for the downstream area and from the cold air brought by the cyclonic circulation anomaly for the area south of the KE.

We summarize the possible physical mechanism underlying the midlevel cooling as follows. Over the KE transition region, the deep-reaching ascending motion induces a strong local

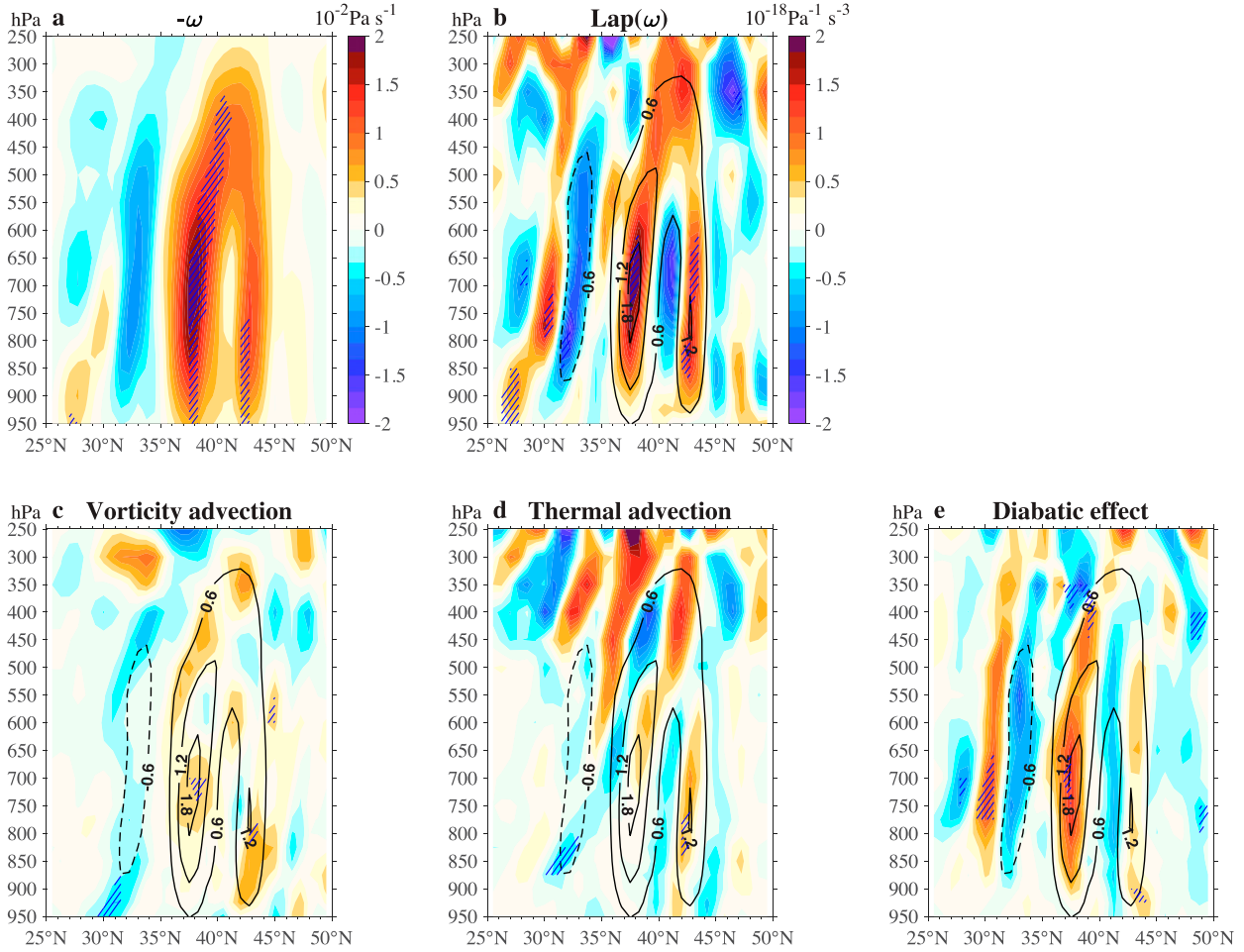


FIG. 11. Latitude–pressure sections of 155°–165°E zonal-mean regressions (colors) of (a) sign-reversed vertical velocity $-\omega$ ($10^{-2} \text{ Pa s}^{-1}$) and (b)–(e) terms in the modified quasigeostrophic ω equation [see Eq. (9) for detail; $10^{-18} \text{ Pa}^{-1} \text{ s}^{-3}$] in January against SST-EC_{Nov}. Black contours in (b)–(e) are repeats of (a). Hatching indicates regression is significant at the 90% confidence level.

adiabatic cooling, which is then advected away by the background northwesterly wind, leading to the midlevel cooling on a broader scale that causes the southward shift of baroclinicity and thereby the displaced storm tracks.

d. Attribution of ascending motion

What drives the critical anomalous updraft that leads to a series of thermodynamic changes mentioned above? We consider a modified quasigeostrophic ω equation that takes into account the diabatic effect (Smirnov et al. 2015; Gu et al. 2018):

$$\left(\sigma \nabla^2 + f^2 \frac{\partial^2}{\partial p^2} \right) \omega = f \frac{\partial}{\partial p} [\mathbf{V}_g \cdot \nabla (\zeta_g + f)] + \frac{R_d}{p} \nabla^2 (\mathbf{V}_g \cdot \nabla T) - \frac{\kappa}{p} \nabla^2 Q, \quad (9)$$

where σ is the background static stability parameter as defined in (3), and \mathbf{V}_g and ζ_g are geostrophic wind vector and relative vorticity of the geostrophic wind, respectively. The

terms on the rhs of (9) represent the effects of vorticity advection, thermal advection and diabatic heating effect. A positive (negative) rhs term accompanies a positive (negative) Laplacian ω [the lhs of (9) is referred to as $\text{Lap}(\omega)$], implying a negative (positive) ω corresponding to an upward (downward) motion. Here we compute the monthly mean field of each term using the 6-hourly data to qualitatively diagnose the relative importance of the dynamic and thermodynamic effects to the ω response.

Figure 11 shows the latitudinal–vertical section of the 155°–165°E zonal-mean response of the upward vertical motion ($-\omega$) and each term of (9). The narrowness of anomalous ascending and descending motions are well represented by the $\text{Lap}(\omega)$ response (Figs. 11a,b), demonstrating that the quasigeostrophic $\text{Lap}(\omega)$ is a good approximation to the local extrema of $-\omega$. Comparing the responses of $\text{Lap}(\omega)$ and other terms shown in (Figs. 11c–e), it is evident that change in differential diabatic heating is the key factor in determining the $\text{Lap}(\omega)$ response from 900 to 400 hPa. The effects of vorticity advection and thermal advection are

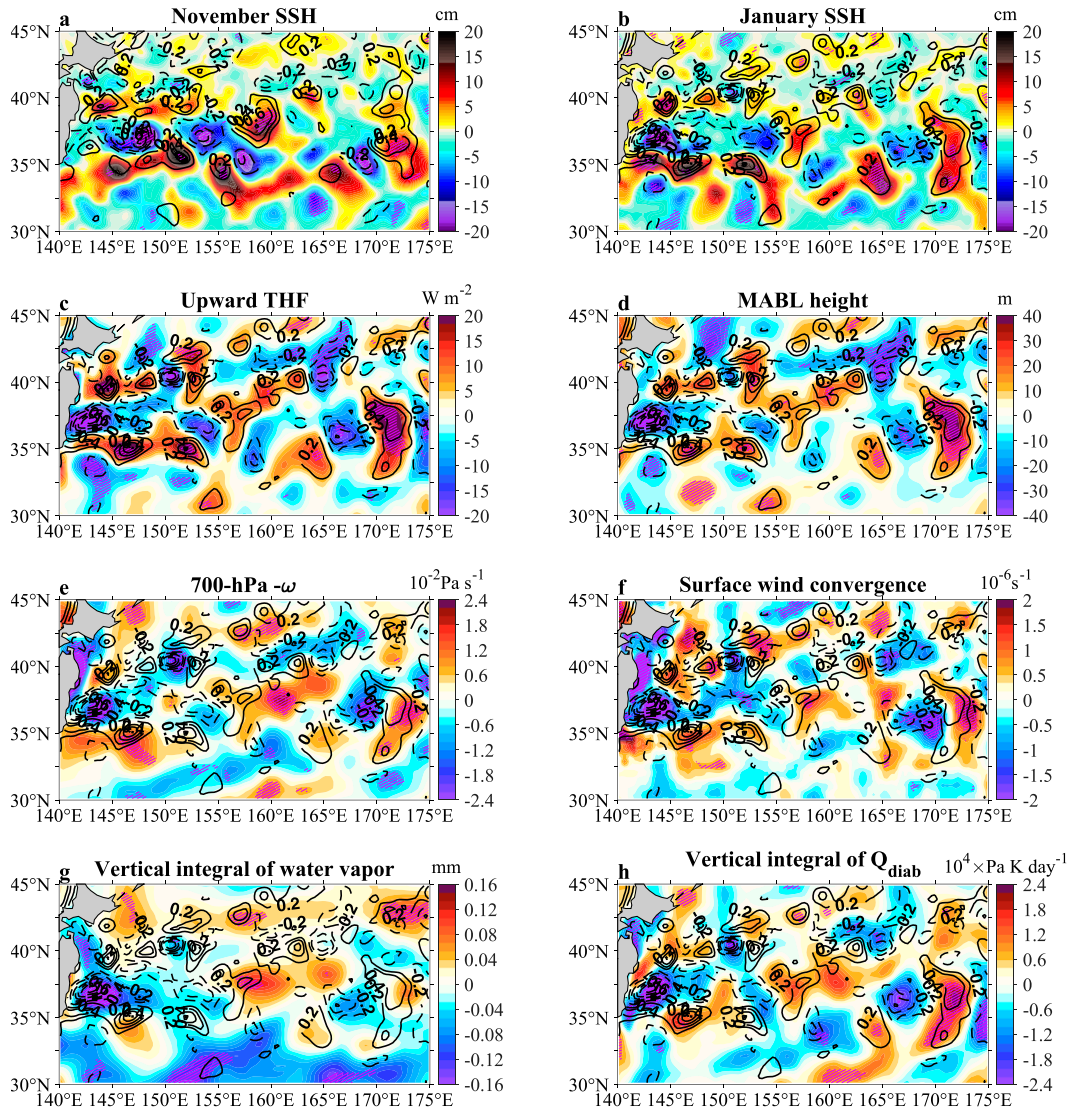


FIG. 12. Mesoscale responses (colors) of SSH (cm) in (a) November and (b) January, and of (c) upward turbulent heat flux (W m^{-2}), (d) MABL height (m), (e) 700-hPa $-\omega$ ($10^{-2} \text{ Pa s}^{-1}$), (f) surface wind convergence (10^{-6} s^{-1}), (g) vertical integral (over the entire atmosphere) of water vapor (mm), and (h) vertical integral (from 1000 to 100 hPa) of diabatic heating rate ($10^4 \text{ Pa K day}^{-1}$) in January. Black contours denote the mesoscale responses of SST in November in (a) and January in (b)–(h). Hatching indicates regression is significant at the 90% confidence level. Here the MABL height is defined as the lowest level at which the bulk Richardson number reaches the critical value of 0.25.

actually much less important in the KE transition region. Although the response amplitude of diabatic heating itself is not substantially larger than that of the mean horizontal advection (cf. Figs. 8a,g), it is the greater spatial heterogeneity of the former that earns its predominance. The importance of the finer-scale structure of diabatic heating has been emphasized by Willison et al. (2013) for the better simulation of cyclogenesis and by Smirnov et al. (2015) for the stronger vertical motion in high-resolution AGCM experiment than in low-resolution experiment. We note that for the area south of the KE, differential cold advection

primarily induces the anomalous descent, as manifested in the collocation of the adiabatic warming with the cold air advection (cf. Figs. 10a,c). In short, the result suggests that the finer-scale increase of diabatic heating confined to the downstream transition region acts to facilitate ascending motion reaching deep into the upper troposphere. We conjecture that mesoscale warm SST anomalies drive the increased diabatic heating and the anomalous ascending motion in the first place, penetrating into the free atmosphere above the MABL. This will be illustrated in the next subsection.

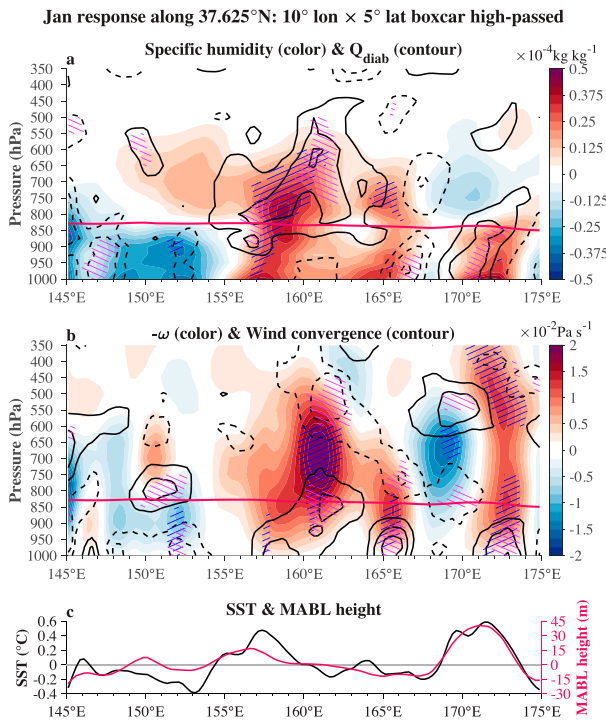


FIG. 13. Longitude–pressure sections of mesoscale responses of (a) specific humidity (colors; $10^{-4} \text{ kg kg}^{-1}$) and diabatic heating rate (contour interval is every 0.2 K day^{-1} from $\pm 0.2 \text{ K day}^{-1}$) and (b) sign-reversed vertical velocity $-\omega$ (colors; $10^{-2} \text{ Pa s}^{-1}$) and horizontal wind convergence (contour interval is every $0.4 \times 10^{-6} \text{ s}^{-1}$ from $\pm 0.4 \times 10^{-6} \text{ s}^{-1}$) along 37.625°N in January. Thick red lines in (a) and (b) indicate the MABL height. Blue (red) hatching indicates regression represented by colors (contours) is significant at the 90% confidence level. (c) The corresponding longitudinal transects of mesoscale responses of SST (black line; $^\circ\text{C}$) and MABL height (red line; m).

e. Marine atmospheric boundary layer response

To isolate the air–sea coupling associated with mesoscale SST anomalies, we apply a 10° longitude \times 5° latitude high-pass boxcar filter to both oceanic and atmospheric fields, following Koseki and Watanabe (2010). The ratio of the filtered to unfiltered SST power spectrum shows a half-power wavelength of around 600 km (not shown), confirming that SST variance is retained at mesoscale. Here mesoscale anomalies are loosely referred to as perturbations associated with oceanic eddies and fronts, since they cannot be distinguished by the spatial filter. In the rest of this subsection, the regression field after spatially high-pass filtering is referred to as the mesoscale response.

As can be seen from Fig. 12a, the mesoscale warm (cold) SST anomalies are clearly visible along with positive (negative) SSH anomaly loops, suggesting that the mesoscale disturbances constitute an essential part of the decadal change in the KE system, especially for the critical downstream warm SST anomalies. Compared with the downstream SST/SSH responses in November, such as positive anomalies around 160° and 172.5°E , the responses appear

to locate farther westward with distorted shapes and persistent amplitudes in January (Fig. 12b), reflecting the progression of SST anomalies associated with long-lived eddies from November to January. The mesoscale warm SST anomalies in January coincide with the peaks of unfiltered SST regression (not shown). They are accompanied with intense turbulent heat release from ocean (Fig. 12c), which heats the overlying near-surface air and results in higher-than-normal MABL (Fig. 12d). Particularly looking at the downstream transition region, surface wind mainly converges above the eastern edge of SST warm core and the ascending motion occurs slightly downstream (Figs. 12e,f). Correspondingly, increases in the vertically integrated water vapor and diabatic heating are evident in the vicinity of warm anomalies (Figs. 12g,h). These features are consistent with the modeled local atmospheric response to the idealized mesoscale oceanic warm eddies in the KE transition region (Sugimoto et al. 2017).

Figure 13 shows the vertical profiles of the mesoscale SST and atmospheric responses along 37.625°N . The MABL height variations roughly follow the mesoscale SST disturbances in the downstream area (Fig. 13c). Over the SST positive peaks, particularly around 157°E , the specific humidity anomalies have peaks at the sea surface and near the top of MABL (Fig. 13a), indicating more moisture supply from the mesoscale warmer water. Such increased moisture content facilitates strong diabatic heating penetrating into the free atmosphere. Meanwhile, wind convergence extends to the top of MABL with larger amplitude closer to the sea surface, which is collocated with a considerable vertical extent of strong ascending motion (Fig. 13b). It is expected that surface wind convergence induces ascending motion penetrating MABL, which is conducive to the low-level diabatic heating in the presence of abundant moisture supply. The mutual reinforcement between the anomalous ascending motion and diabatic heating makes them reach deep into the upper troposphere.

The MABL wind adjustment to the frontal or mesoscale SST can be explained by two prominent mechanisms: the vertical mixing mechanism (VMM; Wallace et al. 1989) whereby warmer SST destabilizes the overlying atmosphere, enhancing downward transfer of momentum and thus accelerating the surface wind; the pressure adjustment mechanism (PAM; Lindzen and Nigam 1987) whereby local SST maxima induce local surface pressure minima via hydrostatic effect. Masunaga et al. (2016) found that the anomalous SST front in the KE upstream area, which is associated with the KE jet state difference, modulates air–sea fluxes and MABL structure such as surface wind convergence and SLP through both PAM and VMM. They also documented an anomalous ascent reaching $\sim 750 \text{ hPa}$ over positive SST anomalies. Here we focus on the effectiveness of these two mechanisms in the modulation of MABL wind fields by downstream mesoscale SST anomalies which are connected to decadal change in the KE state.

Following previous studies (e.g., Maloney and Chelton 2006; Putrasahan et al. 2013), the effectiveness of VMM is assessed based on the linear relationship between downwind (crosswind)

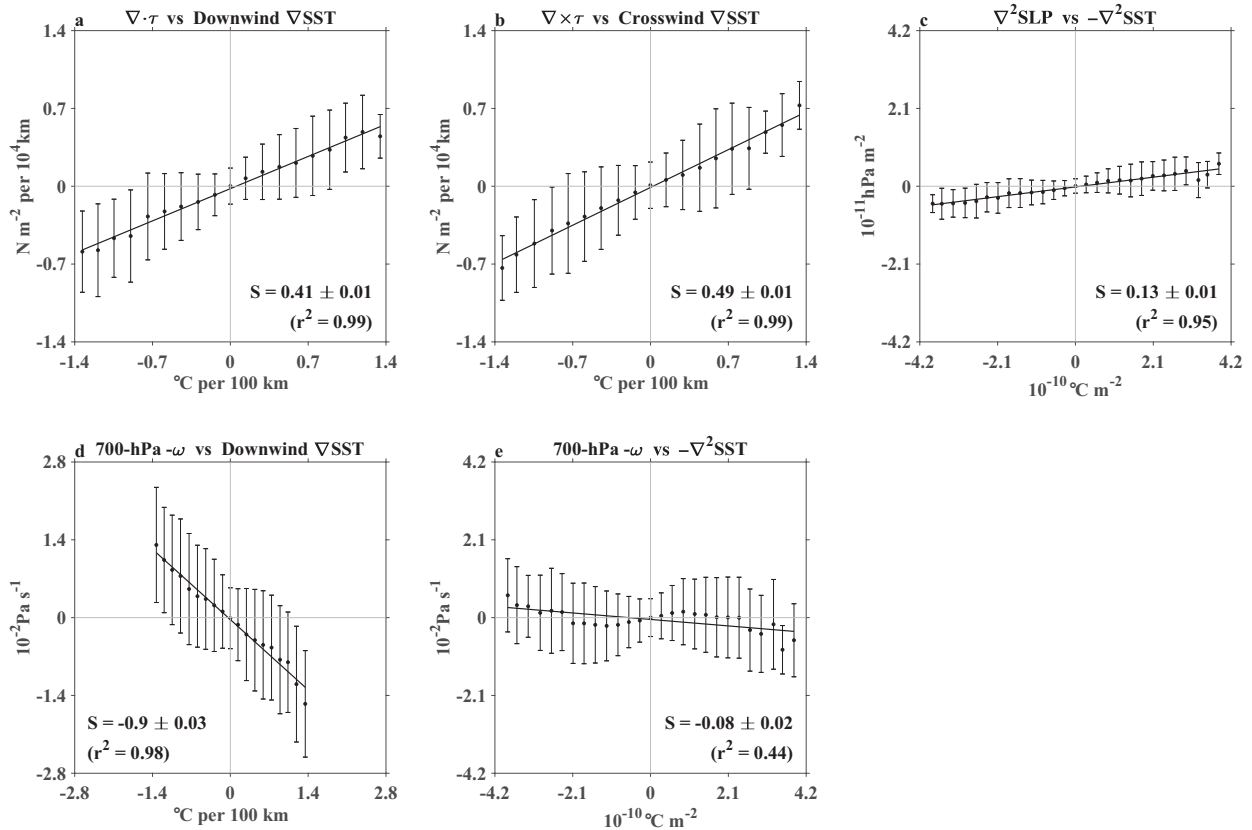


FIG. 14. (a) Binned scatterplot of mesoscale wind stress divergence binned by mesoscale downwind SST gradient in 150° – 170°E , 35° – 40°N , obtained from their reconstruction fields in January associated with SST-EC_{Nov}. Point and error bar denote the mean value and the ± 1 standard deviation of each bin. The straight line denotes a linear fit to these points, of which the slope (S) \pm standard error is shown in the corner of each panel, followed by the squared correlation coefficient (r^2) in parentheses. (b)–(e) As in (a), but for wind stress curl vs crosswind SST gradient in (b), Laplacian SLP vs negative Laplacian SST in (c), 700-hPa $-\omega$ vs downwind SST gradient in (d), and 700-hPa $-\omega$ vs negative Laplacian SST in (e). The unit of each variable is labeled along the corresponding axis.

SST gradient and wind stress divergence (curl) estimated from binned scatterplots. The spatially high-passed monthly fields in January reconstructed against SST-EC_{Nov} are used to form the binned scatterplots. Specifically, Fig. 14 is plotted using time-varying monthly fields associated with SST-EC_{Nov} instead of stationary fields of regression coefficients, and thus the error bar indicates both temporal and spatial spread. As shown in Figs. 14a and 14b, the wind stress divergence (curl) is well correlated with the mesoscale downwind (crosswind) SST gradient ($r^2 = 0.99$), confirming that VMM operates actively. The coupling strength or slope (S) of both metrics is comparable to the observational estimations (Maloney and Chelton 2006). With the same approach, a high correlation between negative Laplacian SST and Laplacian SLP is detected ($r^2 = 0.95$; Fig. 14c), suggesting that PAM could also be at work (Minobe et al. 2008; Masunaga et al. 2016).

The above results indicate a joint presence of VMM and PAM in association with the decadal KE variations, which is consistent with Masunaga et al. (2016). But to what

extent they are responsible for the aforementioned vertical motion response is unclear. We evaluate the linear relationship between downwind SST gradient (negative Laplacian SST), which is key for wind convergence in VMM (PAM), and $-\omega$ at 700 hPa where ascending motion is the strongest. The relationship between $-\omega$ response and downwind SST gradient exhibits great linearity (Fig. 14d), with r^2 (0.98) being substantially larger than that related to the negative Laplacian SST (0.44; Fig. 14e), suggesting the dominant role of VMM in driving the vertical motion response. This is in line with the finding that the collocation of surface wind convergence and ascending motion emerges over the downstream side of SST anomalies (cf. Fig. 13b). In support of this point, Chen et al. (2017) reported that such a type of atmospheric response amounts to 60% of total response to oceanic mesoscale eddies under the prevailing northwesterly wind, whereas the PAM-related type only amounts to 10%. Using eddy-resolving coupled global climate model, Tang et al. (2021) also pointed out the main role played by VMM in wintertime mesoscale surface wind-

SST coupling in the KE region. In addition, [Putrasahan et al. \(2013\)](#) found that VMM relationship between crosswind SST gradient and wind stress curl is a unique feature for mesoscale eddies. Nevertheless, more detailed analysis such as momentum budget diagnosis and model experiments are in need to better understand the vertical motion in response to mesoscale eddies.

5. A delayed negative feedback onto KE variations

We now investigate the potential feedback of the atmospheric response onto the KE system. As mentioned in the introduction, an idea of wind-driven adjustment is well received for explaining the bimodal fluctuations of KE system at decadal time scale. Following previous studies ([Qiu and Chen 2010](#); [Qiu et al. 2014](#)), we examine the relationship between the KE SSH and the North Pacific wind stress curl (WSC) fields associated with the KE decadal variability. [Figure 15a](#) shows time–longitude section of correlation between the SSH anomaly along the KE latitudinal band (31° – 36° N) and the KEI lagging by 0–8 years. It is clearly visible that the anomalous SSH signals emerge in the central North Pacific (175° – 150° W) ~ 4 years earlier and then propagate westward into the upstream KE region. Moreover, the correlation map of WSC at 4-yr lead ([Fig. 15b](#)) shows anomalously negative WSC in the central part of the KE latitudinal band that forces anomalously positive SSH (cf. [Fig. 15a](#)) via local Ekman flux convergence. In view of the identified basin-scale cyclonic circulation in response to the anomalous SST associated with the KE stable state (cf. [Fig. 2d](#)), anomalously positive WSC is expected to emerge and cause the reversal of wind stress forcing. As can be seen from [Fig. 15c](#), the WSC response in January has positive correlation with SST-EC_{Nov} particularly to the south of the long-term-mean WSC zero line over the central-to-eastern basin, indicating wind-driven negative SSH signals concurrently. Indeed, the corresponding SSH correlation map ([Fig. 15d](#)) shows significant negative correlations mainly covering the longitudinal band (165° – 140° W). Note that the grid spacing of WSC is coarser than SSH, making them imperfectly matching. Those wind-driven negative SSH signals in 31° – 36° N would propagate westward into the upstream KE region with a delay of ~ 4 years and subsequently act to weaken the southern recirculation gyre and switch the KE system to the unstable dynamic state, which is consistent with the results of previous studies ([Qiu et al. 2014](#); [Joh and Di Lorenzo 2019](#); [Nonaka et al. 2020](#)).

6. Discussion and summary

At the time of starting the present study, the newly developed high-resolution (0.25° horizontal grid spacing) ECMWF reanalysis dataset ERA5 ([Hersbach et al. 2020](#)) was not publicized. We confirmed almost identical results derived from ERA5 and ERA-Interim for the period 2002–16. We also applied the time-lagged MCA to the North Pacific SLP anomalies (30° – 55° N, 140° E– 120° W) fixed in January with SSH anomalies confined to the broad

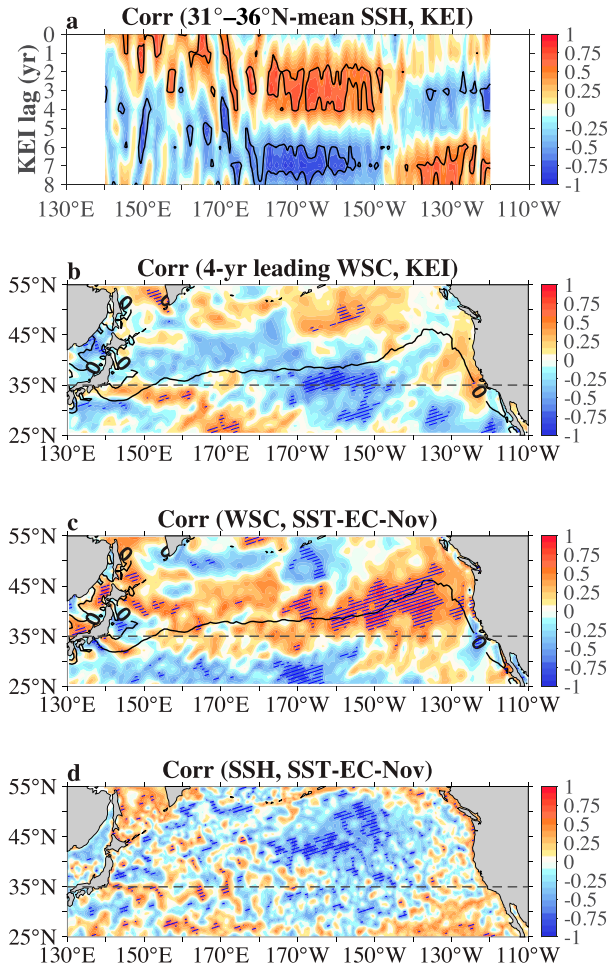


FIG. 15. (a) Lagged correlation between 31° and 36° N meridional-mean SSH anomalies and the wintertime KEI as a function of SSH longitude and time (year) by which KEI lags SSH. Black contours denote correlation significant at the 90% confidence level. (b) Lagged correlation between the wintertime KEI and wind stress curl (WSC) leading by 4 years, with zero line of WSC (black contour). (c) Lagged correlation between SST-EC_{Nov} and the January WSC. (d) As in (c), but for SSH map. Dashed gray lines in (b)–(d) mark 35° N.

KE region (30° – 45° N, 140° – 175° E) leading or lagging by 0–3 months, using the satellite altimetry and ERA5 in the period 1993–2019. [Figure 16a](#) shows that the squared covariance of the first MCA mode is maximized and of unique significance when the November SSH anomalies lead the ensuing January SLP anomalies, with the corresponding expansion coefficients of both SSH and SLP displaying near-decadal variations ($r = 0.79$; [Fig. 16b](#)). The SST and SSH anomaly patterns associated with the SSH expansion coefficients ([Fig. 16c](#)) bear a resemblance to the patterns shown in [Figs. 2a](#) and [2b](#) that delineate the KE stable state, with pattern correlation coefficients of 0.81 and 0.85 for SST and SSH in the broad KE region, respectively. The responses of SLP and Z250 also feature the

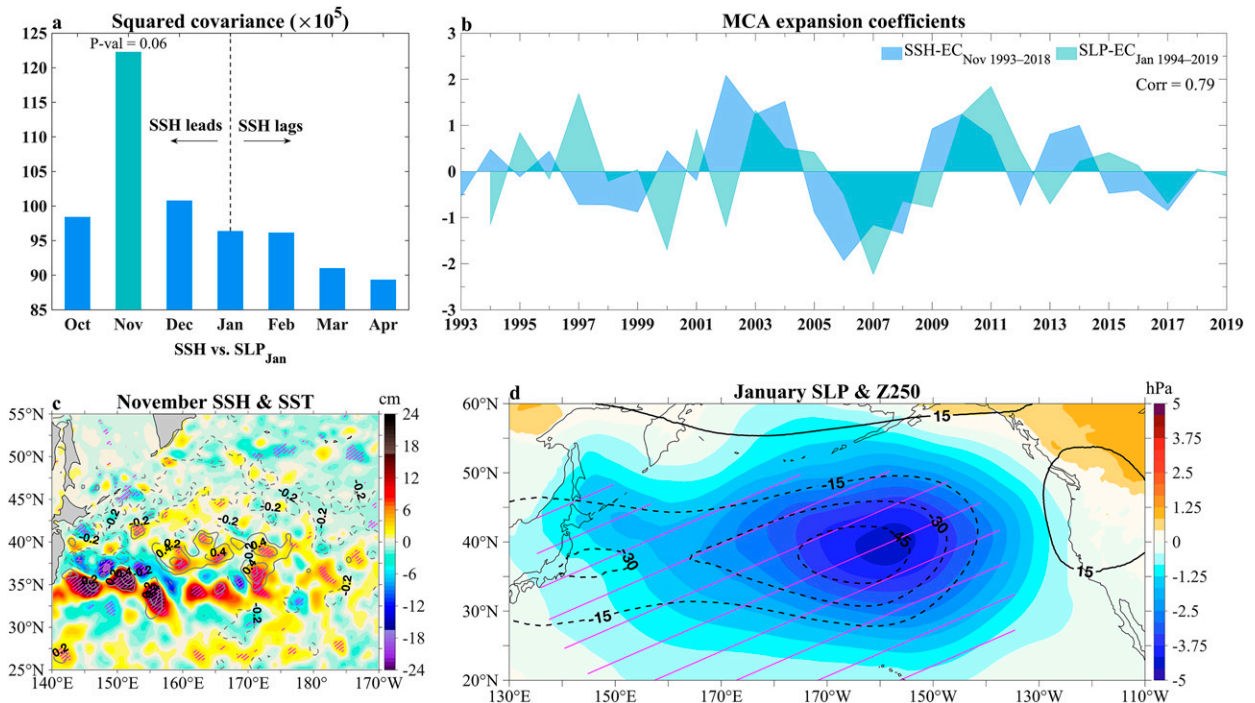


FIG. 16. (a) Squared covariances ($\times 10^5$; dimensionless) of the first MCA modes associated with the January SLP anomalies (30° – 55°N , 140°E – 120°W) and the SSH anomalies (30° – 45°N , 140° – 175°E) leading or lagging by 0–3 months. The abscissa denotes calendar months of SSH. Value significant at the 90% confidence level based on the Monte Carlo test is colored in cyan. (b) The normalized expansion coefficients of SSH in November (SSH-EC_{Nov}; blue) and SLP in the ensuing January (cyan). Regressions onto SSH-EC_{Nov} of (c) SSH (colors; cm) and SST (gray contours; $^{\circ}\text{C}$) in November, and (d) of SLP (colors; hPa) and Z250 (black contours; m) in January. Regressions plotted with contours and hatching are significant at the 90% confidence level.

equivalent-barotropic cyclonic circulation anomaly at basin scale (Fig. 16d), with a local trough above the KE transition region and the low pressure center over the eastern basin shifting slightly to the west of the similar center shown in Fig. 2d. Overall, the resemblance of results associated with the SSH–SLP-derived MCA and the SST–SLP-derived MCA based on different datasets and temporal coverage gives credence to the present findings.

An open question arises as to why the atmospheric responses predominantly show up in January. One possible mechanism is that the sensitivity of transient eddy feedback to the background flow likely causes the subseasonality of atmospheric responses (Peng et al. 1997; Taguchi et al. 2012). In addition to this atmospheric intrinsic sensitivity, we conjecture that air–sea turbulent heat exchanges in the KE region may be dependent on the subseasonal background wind such that the oceanic imprints on MABL could be sensitive. To shed some light on it, Fig. 17 shows the regression maps against SST-EC_{Nov} of SST and turbulent heat flux from November to February, superimposed on the background wind vector in individual months. It is evident that the background wind changes from the westerly in November to the northwesterly in the ensuing three months, with wind speed maximized in January and then somewhat relaxed in February. Correspondingly, the upward turbulent heat flux anomalies are largest in

January in the context of the strongest northwesterly which brings colder and drier air masses to boost ocean heat release, whereas warm SST anomalies evolve slowly. The prevailing northwesterly wind associated with the most intense turbulent heat release to atmosphere in the KOE region has been reported recently (Ogawa and Spengler 2019; Tomita et al. 2021). Such a background northwesterly wind blowing from cold to warm SST could make the vertical momentum mixing more effective in driving the MABL response (Kilpatrick et al. 2014). The specific mechanism is beyond the scope of the present study and in-depth investigation is in need to verify the above hypothesis.

In summary, we propose a coupled ocean–atmosphere delayed oscillator for the decadal variations of the KE dynamic system, in which the wintertime finer-scale thermodynamic response to mesoscale SST anomalies in the KE transition region and slow oceanic baroclinic adjustment are key processes. As illustrated in Fig. 18, when the KE system is in the stable dynamic state, the downstream transition region is filled with the warm SST anomalies associated with mesoscale eddies. The mesoscale warmer water induces intense turbulent heat release to atmosphere and supplies more moisture. Meanwhile, surface wind converges above the downstream side of SST warm core probably via enhanced turbulent mixing within MABL, causing

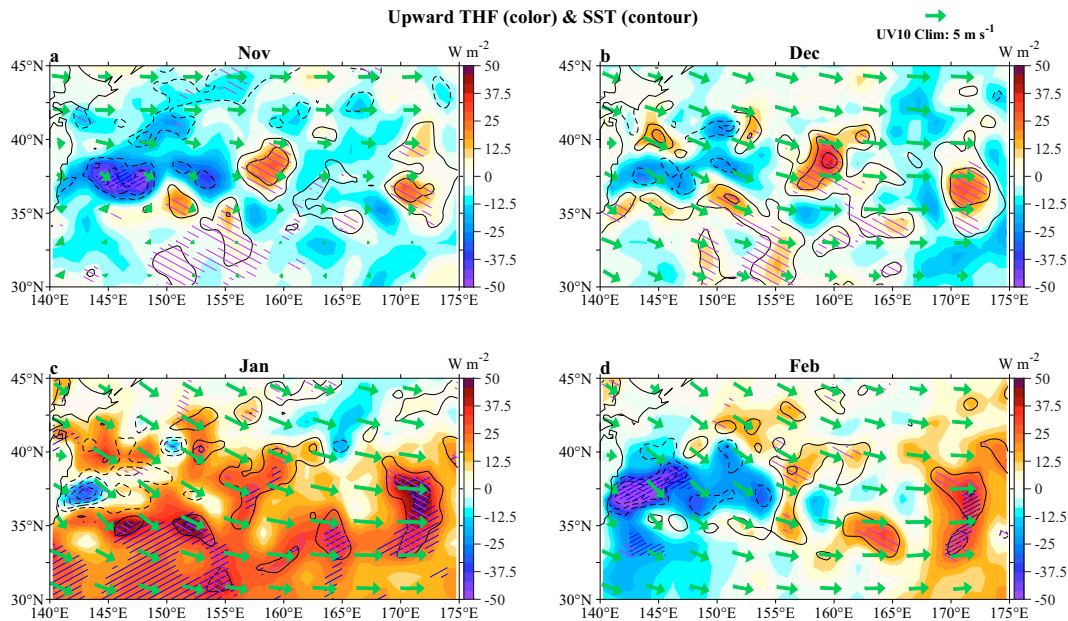


FIG. 17. (a) Regressions onto SST-EC_{Nov} of upward turbulent heat flux (colors; W m^{-2}) and SST (contour interval is every 0.4°C from $\pm 0.4^{\circ}\text{C}$) in November, overlaid with the corresponding 10-m wind (arrows; m s^{-1}) climatology of 1979–2016. (b)–(d) As in (a), but for December, January, and February, respectively. Blue (purple) hatching indicates regression represented by colors (contours) is significant at the 90% confidence level.

ascending motion and strong diabatic heating penetrating into the free atmosphere in the presence of abundant moisture supply. The finer-scale increase of diabatic heating in space likely facilitates the anomalous updraft reaching deep into the upper troposphere. Over the KE transition region, the deep-reaching ascending motion induces a strong local adiabatic cooling, which is then advected away by the background northwesterly wind to spread out. With such cooling, local EAPE production by baroclinic conversion shifts southward, leading to the southward migration of synoptic eddy activity. Concurrently, EAPE production by the synoptic diabatic conversion increases farther downstream, which is conducive to the deflected synoptic eddy activity extending to the eastern basin. The southward-deflected synoptic eddy activity fosters the equivalent-barotropic cyclonic circulation anomaly at basin scale through the transient eddy feedback forcing from anomalous eddy vorticity and heat fluxes. Such cyclonic anomalies are further maintained by energy conversion from the background state. Subsequently, the wind-driven negative SSH anomalies in the central section of the KE latitudinal band propagate westward into the upstream KE region with a delay of ~ 4 years. This delayed negative feedback switches the KE system to the unstable dynamic state, yielding a decadal-scale cycle.

The aforementioned mesoscale ocean–atmosphere coupled delayed oscillator likely helps wind-driven decadal KE variations to be self-sustained and enhances its potential predictability as suggested by Qiu et al. (2014). There is one caveat that the prediction skill of the KE state transition in practice could be disrupted by the nonlinear intrinsic oceanic processes such as the Kuroshio path fluctuations south of Japan

(Wang et al. 2020). As Qiu et al. (2020) reported, the occurrence of the Kuroshio large meander south of Japan in August 2017 could reset the phase of wind-driven decadal KE variations. Predicting the KE system change remains challenging.

Acknowledgments. We appreciate Young-Oh Kwon for thoughtful comments and suggestions. We also appreciate three anonymous reviewers for their time and numerous comments that helped to improve the manuscript substantially. We also thank the Center for High Performance Computing and System Simulation at Pilot National Laboratory for Marine Science and Technology (Qingdao) for the support of computational resources. B. G. is supported by the National Natural Science Foundation of China (NSFC) Projects (41922039 and 42276016), Laoshan Laboratory (No. LSKJ202202602), and NSFC projects (92258302, 91858102). H. Y. is supported by NSFC Project (42176006). L. Z. is supported by NSFC Project (41906015).

Data availability statement. The ERA-Interim data used in this study are openly available from the ECMWF website at <https://www.ecmwf.int/en/forecasts/datasets/reanalysis-datasets/era-interim>. The ERA5 data are openly available from <https://cds.climate.copernicus.eu/cdsapp#!/dataset/reanalysis-era5-pressure-levels-monthly-means?tab=form>. The SSH product can be downloaded from https://data.marine.copernicus.eu/product/SEALEVEL_GLO_PHY_L4_MY_008_047/services. The OISST data can be accessed from <https://www.ncei.noaa.gov/data/sea-surface-temperature-optimum-interpolation/v2.1/access/avhrr/>.

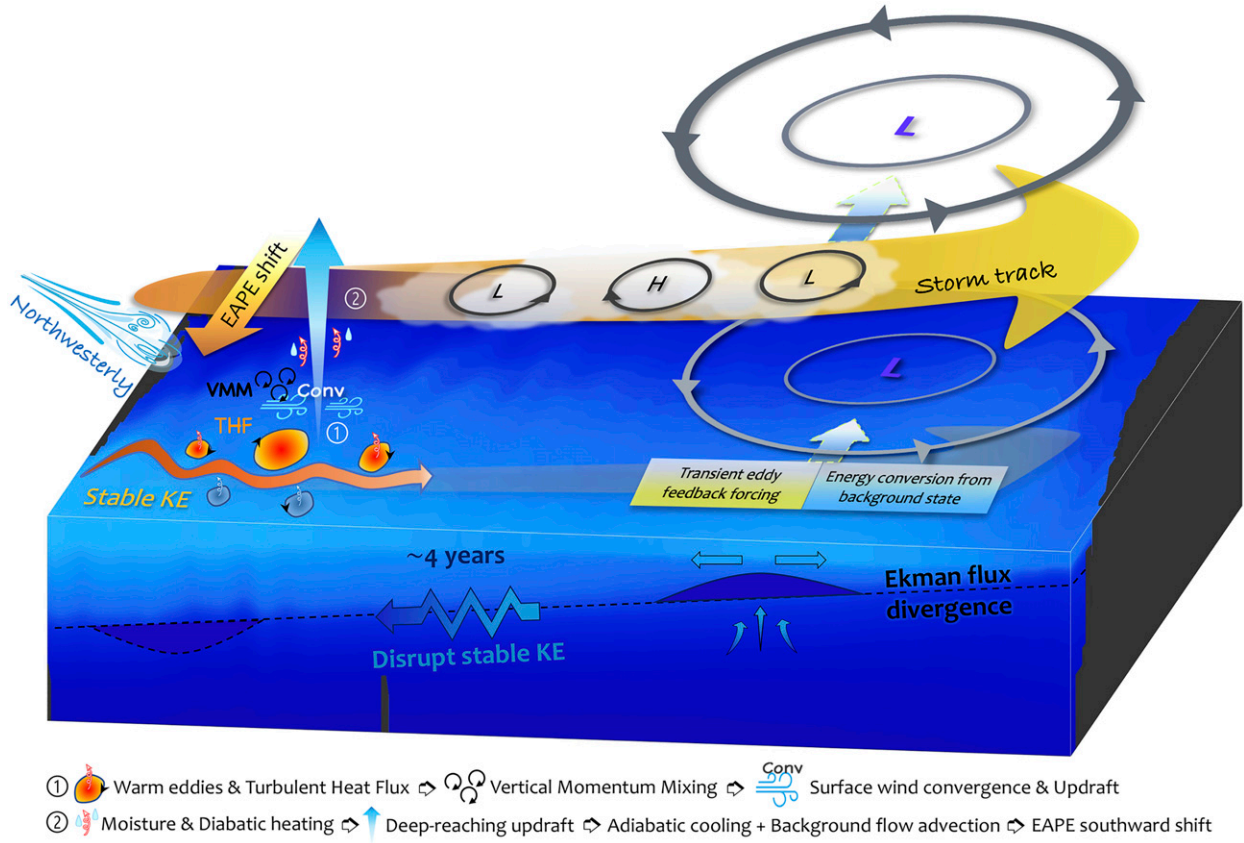


FIG. 18. Schematic of ocean mesoscale activity–atmosphere coupled delayed oscillator for decadal variations of the KE system. During the KE stable state, the responses of MABL processes to the mesoscale oceanic warming associated with the decadal KE variations excite atmospheric thermodynamic adjustments that cause the southward displacement of EAPE and in turn the corresponding change in synoptic eddy activity. The southward deflection of storm tracks in the farther downstream region, fueled by synoptic diabatic production of EAPE, fosters the basin-scale equivalent-barotropic cyclonic circulation anomaly through transient eddy feedback forcing from anomalous eddy vorticity and heat fluxes. Such cyclonic anomaly is further maintained by energy conversion from the background state. The subsequent wind-driven negative SSH anomalies propagate westward into the upstream KE region in ~ 4 years and can trigger the KE unstable state. See section 6 for details.

APPENDIX A

Energetics Analysis for the Maintenance of the Atmospheric Response

To investigate the maintenance processes of the atmospheric circulation response pattern, we examine the conversions of kinetic energy and available potential energy associated with the atmospheric responses to SST-EC_{Nov} in the form as follows (Tanaka et al. 2016; Zhuge and Tan 2021):

$$CP_B = -\frac{R_d}{pS_p} T^* (\mathbf{V}_h^* \cdot \nabla) \hat{T}, \quad (\text{A1})$$

$$CP_Q = \frac{R_d}{pS_p c_p} T^* Q^*, \quad (\text{A2})$$

$$CP_{EH} = -\frac{R_d}{pS_p} T^* [(\mathbf{V}_h' \cdot \nabla) T']^*, \quad (\text{A3})$$

$$CP_K = \frac{R_d}{p} T^* \omega^*, \quad (\text{A4})$$

$$CK_B = -\mathbf{V}_h^* \cdot (\mathbf{V}_3^* \cdot \nabla_3) \hat{\mathbf{V}}_h, \quad (\text{A5})$$

$$CK_{EH} = -\mathbf{V}_h^* \cdot [(\mathbf{V}_3' \cdot \nabla_3) \mathbf{V}_h']^*, \quad (\text{A6})$$

where $S_p = [R_d T / (c_p p)] - (\partial T / \partial p)$ is the static stability with $R_d = 287 \text{ J kg}^{-1} \text{ K}^{-1}$ the dry-air gas constant and $c_p = 1004 \text{ J kg}^{-1} \text{ K}^{-1}$ the air specific heat capacity at constant pressure, subscript 3 denotes the 3D expression, \mathbf{V}_h is the horizontal wind vector, ω is the pressure velocity, and Q is the diabatic heating rate per unit mass. Here asterisks denote monthly anomalies associated with SST-EC_{Nov}, and prime and hat denote the synoptic perturbations and monthly long-term mean, respectively. Equations (A1)–(A4) describe generation and conversion terms of available potential energy $\{[R_d / (pS_p)] [(T^*)^2 / 2]\}$. CP_B is the baroclinic energy

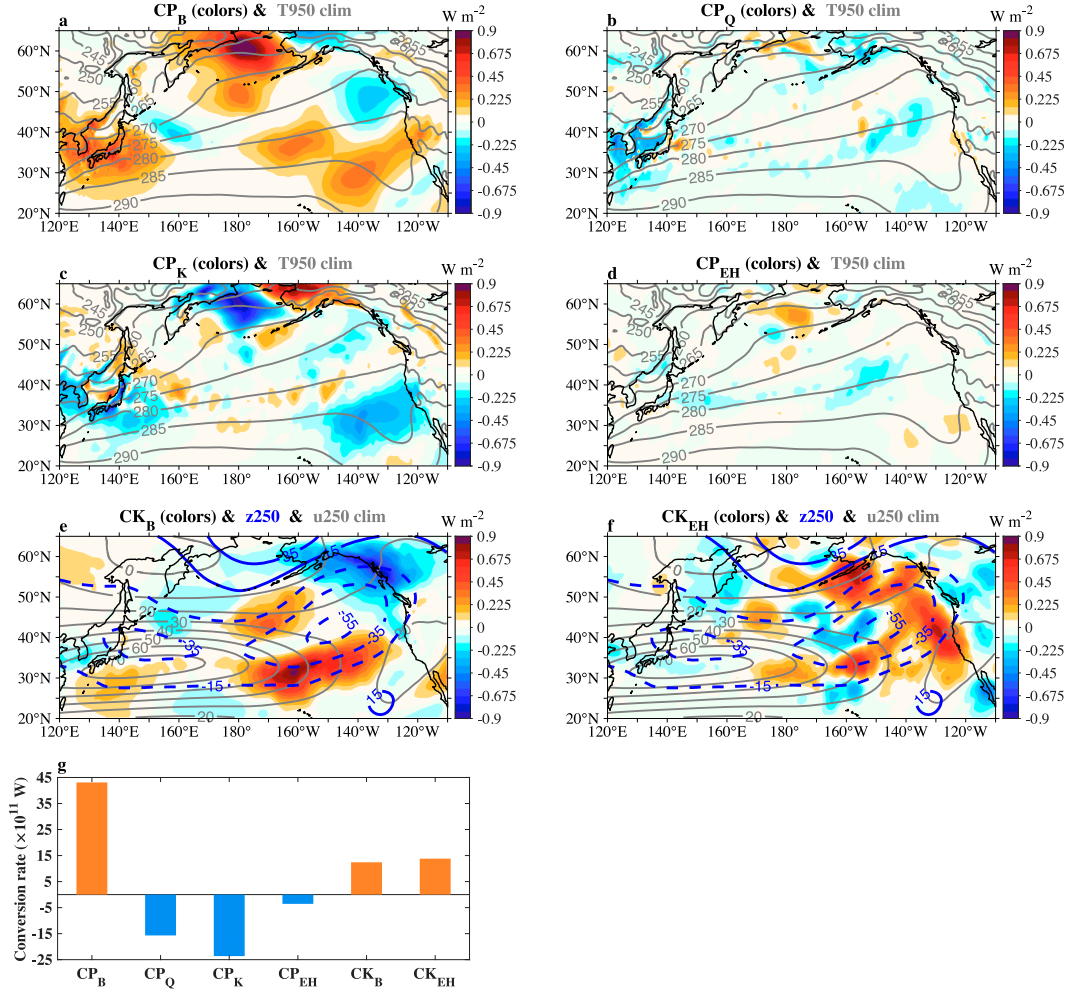


FIG. A1. (a) Vertical integral of CP_B (colors; W m^{-2}), overlaid with the long-term mean of 950-hPa air temperature (gray contours; K) in January. (b)–(d) As in (a), but for CP_Q , CP_K , and CP_{EH} , respectively (color shading). (e) Vertical integral of CK_B (colors; W m^{-2}), overlaid with regressions of Z250 (blue contours; m) onto SST-EC_{Nov} and long-term mean of 250-hPa zonal wind (gray contours; m s^{-1}) in January. (f) As in (e), but for CK_{EH} (colors). (g) Vertically and horizontally integrated CP_B , CP_Q , CP_K , CP_{EH} , CK_B , and CK_{EH} ($\times 10^{11} \text{ W}$). The horizontal and vertical domain for integration is $(120^\circ\text{E}–110^\circ\text{W}, 20^\circ–65^\circ\text{N})$ and 1000–100 hPa, respectively. See Eqs. (A1)–(A6) for details on energy conversion terms.

conversion from the background state into monthly anomalies. CP_Q is the diabatic generation. CP_{EH} is the baroclinic transient eddy feedback. CP_K is conversion from kinetic energy to available potential energy. Equations (A5) and (A6) describe conversions of kinetic energy $[\mathbf{V}_h^* \cdot \mathbf{V}_h^*/2]$. CK_B is the barotropic energy conversion from the background mean flow into monthly anomalies. CK_{EH} is the barotropic transient eddy feedback.

Figures A1a–f show distributions of vertically integrated energy conversion terms. The distribution of pronounced CP_B values (Fig. A1a) is evidently consistent with the advection of background air temperature by anomalous circulation (cf. blue contours in Fig. A1e). It also coincides well with the CP_K pattern with the sign reversed (Fig. A1c), indicating that CP_K converts part of

the energy gain of CP_B to kinetic energy. CP_Q and CP_{EH} are relatively weak, with stronger damping caused by CP_Q than by CP_{EH} (Figs. A1b,d). As for conversions of kinetic energy, CK_B is mainly pronounced in the jet exit region and over the western coast of Canada (Fig. A1e). Further inspection (not shown) reveals that the positive CK_B around the southern flank of the jet and the negative CK_B over the western coast of Canada are contributed by $-u^*u^*(\partial\hat{u}/\partial x)$, where anomalous zonal advection of background westerly momentum acts on the anomalous zonal wind itself; the positive CK_B around the northern flank of the jet results from $-u^*v^*(\partial\hat{u}/\partial y)$, where anomalous poleward flux of westerly momentum across the meridional shear of the jet reinforces the anomalous flow. CK_{EH} is mainly pronounced in the downstream region (Fig. A1f), and its

horizontal distribution is generally consistent with the upper-level geopotential height tendency induced by eddy vorticity forcing (cf. Fig. 4).

As indicated in Fig. A1g, CP_B contributes most efficiently to maintaining the available potential energy associated with the atmospheric response pattern. About 55% of CP_B converts into kinetic energy through CP_K , and part of it acts against thermal damping by CP_Q (36%) and CP_{EH} (8%). As for kinetic energy of the pattern, CP_K is the largest energy source, followed by CK_{EH} and CK_B . The total energy gain by synoptic eddy feedback forcing ($CP_{EH} + CK_{EH}$) is 18% of that by energy conversion from the background state ($CP_B + CK_B$). These results show that the detected atmospheric response pattern is largely maintained by the energy conversion from the background state and, to a lesser extent, by synoptic eddy feedback forcing, which is consistent with previous studies (e.g., Tanaka et al. 2016; Okajima et al. 2018; Kim et al. 2021). Nonetheless, note that here the monthly energetics analysis only diagnoses the maintenance processes of atmospheric response pattern rather than its growth and decay processes, in which there may be distinct roles for transient eddies (Zhuge and Tan 2021). It should be also noted that the energy conversion from the background state actually requires preexisting anomalous flow for energy extraction. As it stands, the preexisting anomalies in the context of the present study are associated with the eddy-mediated response to ocean mesoscale activity in the KE transition region.

APPENDIX B

Eddy Temperature Variance Equation

The eddy temperature variance Eq. (5) is derived from the thermodynamic equation in pressure coordinates (Illari and Marshall 1983):

$$\frac{\partial T}{\partial t} + \mathbf{V}_h \cdot \nabla T - S_p \omega = \frac{Q}{c_p}, \quad (\text{B1})$$

where notations conform to previous definitions. We then decompose thermodynamical or dynamical variable X in (B1) into monthly mean \bar{X} , synoptic anomalies X' , and non-synoptic submonthly anomalies X^- ; i.e., $X = \bar{X} + X' + X^-$. We thus obtain

$$\begin{aligned} \frac{\partial(\bar{T} + T' + T^-)}{\partial t} + (\bar{\mathbf{V}}_h + \mathbf{V}'_h + \mathbf{V}^-_h) \cdot \nabla(\bar{T} + T' + T^-) \\ - (\bar{S}_p + S'_p + S^-_p)(\bar{\omega} + \omega' + \omega^-) \\ = \frac{\bar{Q} + Q' + Q^-}{c_p} \end{aligned} \quad (\text{B2})$$

Averaging (B2) over time yields

$$\frac{\partial \bar{T}}{\partial t} + \bar{\mathbf{V}}_h \cdot \nabla \bar{T} - \bar{S}_p \bar{\omega} = \frac{\bar{Q}}{c_p}. \quad (\text{B3})$$

Subtracting (B3) from (B2) yields

$$\begin{aligned} \frac{\partial T'}{\partial t} + \bar{\mathbf{V}}_h \cdot \nabla T' + \mathbf{V}'_h \cdot \nabla \bar{T} + \mathbf{V}'_h \cdot \nabla T' - \bar{\mathbf{V}}'_h \cdot \nabla T' \\ - (\bar{S}_p \omega' + S'_p \bar{\omega} + S'_p \omega' - \bar{S}_p \omega') = \frac{Q'}{c_p} + \text{Res}, \end{aligned} \quad (\text{B4})$$

where the residual term Res consists of terms related to X^- . Multiplying (B4) with T' and then time averaging yields

$$\begin{aligned} \frac{\partial}{\partial t} \left(\frac{1}{2} \overline{T'^2} \right) + \bar{\mathbf{V}}_h \cdot \nabla \left(\frac{1}{2} \overline{T'^2} \right) + \overline{\mathbf{V}'_h T'} \cdot \nabla \bar{T} - \overline{\omega' T'} \bar{S}_p - \overline{T' S'_p \omega} \\ = \frac{1}{c_p} \overline{Q' T'} + \text{Res}. \end{aligned} \quad (\text{B5})$$

Substituting the continuity equation and noting the fifth term on the lhs of (B5), we get

$$-\overline{T' S'_p \omega} = - \left[\frac{2\kappa}{p} \left(\frac{1}{2} \overline{T'^2} \right) - \frac{\partial}{\partial p} \left(\frac{1}{2} \overline{T'^2} \right) \right] \bar{\omega},$$

where $\kappa = R_d/c_p$, (B5) can be rewritten as

$$\begin{aligned} \frac{\partial}{\partial t} \left(\frac{1}{2} \overline{T'^2} \right) + \nabla \cdot \nabla \left(\frac{1}{2} \overline{T'^2} \right) + \left(\frac{\partial}{\partial p} - \frac{2\kappa}{p} \right) \left(\frac{1}{2} \overline{\omega T'^2} \right) + \overline{\mathbf{V}'_h T'} \cdot \nabla \bar{T} \\ - \overline{\omega' T' S'_p} = \frac{1}{c_p} \overline{Q' T'} + \text{Res}. \end{aligned} \quad (\text{B6})$$

Given that the tendency term [first term on the lhs of (B6)] is of smaller magnitude compared with other nonresidual terms, we include it into the residual term and rearrange (B6), arriving at (5).

REFERENCES

- Cai, Z., H. Xu, J. Ma, and J. Deng, 2021: Climatic effects of spring mesoscale oceanic eddies in the North Pacific: A regional modeling study. *Atmosphere*, **12**, 517, <https://doi.org/10.3390/atmos12040517>.
- Ceballos, L. I., E. D. Lorenzo, C. D. Hoyos, N. Schneider, and B. Taguchi, 2009: North Pacific Gyre oscillation synchronizes climate fluctuations in the eastern and western boundary systems. *J. Climate*, **22**, 5163–5174, <https://doi.org/10.1175/2009JCLI2848.1>.
- Chang, E. K. M., S. Lee, and K. L. Swanson, 2002: Storm track dynamics. *J. Climate*, **15**, 2163–2183, [https://doi.org/10.1175/1520-0442\(2002\)015<0216:STD>2.0.CO;2](https://doi.org/10.1175/1520-0442(2002)015<0216:STD>2.0.CO;2).
- Chelton, D., and S.-P. Xie, 2010: Coupled ocean–atmosphere interaction at oceanic mesoscales. *Oceanography*, **23**, 52–69, <https://doi.org/10.5670/oceanog.2010.05>.
- Chen, F. F., Q. Chen, H. Hu, J. Fang, and H. Bai, 2020: Synergistic effects of midlatitude atmospheric upstream disturbances and oceanic subtropical front intensity variability on western Pacific jet stream in winter. *J. Geophys. Res. Atmos.*, **125**, e2020JD032788, <https://doi.org/10.1029/2020JD032788>.
- Chen, L., Y. Jia, and Q. Liu, 2017: Oceanic eddy-driven atmospheric secondary circulation in the winter Kuroshio Extension

- region. *J. Oceanogr.*, **73**, 295–307, <https://doi.org/10.1007/s10872-016-0403-z>.
- Choi, D.-H., J.-S. Kug, W.-T. Kwon, F.-F. Jin, H.-J. Baek, and S.-K. Min, 2010: Arctic Oscillation responses to greenhouse warming and role of synoptic eddy feedback. *J. Geophys. Res.*, **115**, D17103, <https://doi.org/10.1029/2010JD014160>.
- Czaja, A., and C. Frankignoul, 2002: Observed impact of Atlantic SST anomalies on the North Atlantic oscillation. *J. Climate*, **15**, 606–623, [https://doi.org/10.1175/1520-0442\(2002\)015<0606:OIOASA>2.0.CO;2](https://doi.org/10.1175/1520-0442(2002)015<0606:OIOASA>2.0.CO;2).
- , —, S. Minobe, and B. Vannière, 2019: Simulating the midlatitude atmospheric circulation: What might we gain from high-resolution modeling of air–sea interactions? *Curr. Climate Change Rep.*, **5**, 390–406, <https://doi.org/10.1007/s40641-019-00148-5>.
- Dee, D. P., and Coauthors, 2011: The ERA-Interim reanalysis: Configuration and performance of the data assimilation system. *Quart. J. Roy. Meteor. Soc.*, **137**, 553–597, <https://doi.org/10.1002/qj.828>.
- Deser, C., R. A. Tomas, and S. Peng, 2007: The transient atmospheric circulation response to North Atlantic SST and sea ice anomalies. *J. Climate*, **20**, 4751–4767, <https://doi.org/10.1175/JCLI4278.1>.
- Ducet, N., P. Y. L. Traon, and G. Reverdin, 2000: Global high-resolution mapping of ocean circulation from TOPEX/Poseidon and ERS-1 and -2. *J. Geophys. Res.*, **105**, 19 477–19 498, <https://doi.org/10.1029/2000JC900063>.
- Fang, J., and X.-Q. Yang, 2016: Structure and dynamics of decadal anomalies in the wintertime midlatitude North Pacific ocean–atmosphere system. *Climate Dyn.*, **47**, 1989–2007, <https://doi.org/10.1007/s00382-015-2946-x>.
- Foussard, A., G. Lapeyre, and R. Plougonven, 2019: Storm track response to oceanic eddies in idealized atmospheric simulations. *J. Climate*, **32**, 445–463, <https://doi.org/10.1175/JCLI-D-18-0415.1>.
- Frankignoul, C., and E. Kestenare, 2005: Air–sea interactions in the tropical Atlantic: A view based on lagged rotated maximum covariance analysis. *J. Climate*, **18**, 3874–3890, <https://doi.org/10.1175/JCLI3498.1>.
- , N. Sennéchal, Y.-O. Kwon, and M. A. Alexander, 2011: Influence of the meridional shifts of the Kuroshio and the Oyashio Extensions on the atmospheric circulation. *J. Climate*, **24**, 762–777, <https://doi.org/10.1175/2010JCLI3731.1>.
- Frenger, I., N. Gruber, R. Knutti, and M. Münnich, 2013: Imprint of Southern Ocean eddies on winds, clouds and rainfall. *Nat. Geosci.*, **6**, 608–612, <https://doi.org/10.1038/ngeo1863>.
- Gan, B., and L. Wu, 2013: Seasonal and long-term coupling between wintertime storm tracks and sea surface temperature in the North Pacific. *J. Climate*, **26**, 6123–6136, <https://doi.org/10.1175/JCLI-D-12-00724.1>.
- , and —, 2015: Feedbacks of sea surface temperature to wintertime storm tracks in the North Atlantic. *J. Climate*, **28**, 306–323, <https://doi.org/10.1175/JCLI-D-13-00719.1>.
- , Y.-O. Kwon, T. M. Joyce, K. Chen, and L. Wu, 2019: Influence of the Kuroshio interannual variability on the summer-time precipitation over the East China Sea and adjacent area. *J. Climate*, **32**, 2185–2205, <https://doi.org/10.1175/JCLI-D-18-0538.1>.
- Gu, W., L. Wang, Z.-Z. Hu, K. Hu, and Y. Li, 2018: Interannual variations of the first rainy season precipitation over South China. *J. Climate*, **31**, 623–640, <https://doi.org/10.1175/JCLI-D-17-0284.1>.
- Hersbach, H., and Coauthors, 2020: The ERA5 global reanalysis. *Quart. J. Roy. Meteor. Soc.*, **146**, 1999–2049, <https://doi.org/10.1002/qj.3803>.
- Hosoda, S., M. Nonaka, Y. Sasai, and H. Sasaki, 2015: Early summertime interannual variability in surface and subsurface temperature in the North Pacific. *J. Oceanogr.*, **71**, 557–573, <https://doi.org/10.1007/s10872-015-0307-3>.
- Illari, L., and J. C. Marshall, 1983: On the interpretation of eddy fluxes during a blocking episode. *J. Atmos. Sci.*, **40**, 2232–2242, [https://doi.org/10.1175/1520-0469\(1983\)040<2232:OTIOEF>2.0.CO;2](https://doi.org/10.1175/1520-0469(1983)040<2232:OTIOEF>2.0.CO;2).
- Joh, Y., and E. Di Lorenzo, 2019: Interactions between Kuroshio Extension and central tropical Pacific lead to preferred decadal-timescale oscillations in Pacific climate. *Sci. Rep.*, **9**, 13558, <https://doi.org/10.1038/s41598-019-49927-y>.
- Kelly, K. A., R. J. Small, R. M. Samelson, B. Qiu, T. M. Joyce, Y.-O. Kwon, and M. F. Cronin, 2010: Western boundary currents and frontal air–sea interaction: Gulf Stream and Kuroshio Extension. *J. Climate*, **23**, 5644–5667, <https://doi.org/10.1175/2010JCLI3346.1>.
- Kida, S., and Coauthors, 2015: Oceanic fronts and jets around Japan: A review. *J. Oceanogr.*, **71**, 469–497, <https://doi.org/10.1007/s10872-015-0283-7>.
- Kilpatrick, T., N. Schneider, and B. Qiu, 2014: Boundary layer convergence induced by strong winds across a midlatitude SST front. *J. Climate*, **27**, 1698–1718, <https://doi.org/10.1175/JCLI-D-13-00101.1>.
- Kim, M., C. Yoo, M.-K. Sung, and S. Lee, 2021: Classification of wintertime atmospheric teleconnection patterns in the Northern Hemisphere. *J. Climate*, **34**, 1847–1861, <https://doi.org/10.1175/JCLI-D-20-0339.1>.
- Koseki, S., and M. Watanabe, 2010: Atmospheric boundary layer response to mesoscale SST anomalies in the Kuroshio Extension. *J. Climate*, **23**, 2492–2507, <https://doi.org/10.1175/2009JCLI2915.1>.
- Kouketsu, S., H. Tomita, E. Oka, S. Hosoda, T. Kobayashi, and K. Sato, 2012: The role of meso-scale eddies in mixed layer deepening and mode water formation in the western North Pacific. *J. Oceanogr.*, **68**, 63–77, <https://doi.org/10.1007/s10872-011-0049-9>.
- Kushnir, Y., W. A. Robinson, I. Bladé, N. M. J. Hall, S. Peng, and R. Sutton, 2002: Atmospheric GCM response to extratropical SST anomalies: Synthesis and evaluation. *J. Climate*, **15**, 2233–2256, [https://doi.org/10.1175/1520-0442\(2002\)015<2233:AGRTES>2.0.CO;2](https://doi.org/10.1175/1520-0442(2002)015<2233:AGRTES>2.0.CO;2).
- Kuwano-Yoshida, A., and S. Minobe, 2017: Storm-track response to SST fronts in the northwestern Pacific region in an AGCM. *J. Climate*, **30**, 1081–1102, <https://doi.org/10.1175/JCLI-D-16-0331.1>.
- Kwon, Y.-O., and T. M. Joyce, 2013: Northern Hemisphere winter atmospheric transient eddy heat fluxes and the Gulf Stream and Kuroshio–Oyashio Extension variability. *J. Climate*, **26**, 9839–9859, <https://doi.org/10.1175/JCLI-D-12-00647.1>.
- , M. A. Alexander, N. A. Bond, C. Frankignoul, H. Nakamura, B. Qiu, and L. A. Thompson, 2010: Role of the Gulf Stream and Kuroshio–Oyashio systems in large-scale atmosphere–ocean interaction: A review. *J. Climate*, **23**, 3249–3281, <https://doi.org/10.1175/2010JCLI3343.1>.
- Lau, N.-C., and E. O. Holopainen, 1984: Transient eddy forcing of the time-mean flow as identified by geopotential tendencies. *J. Atmos. Sci.*, **41**, 313–328, [https://doi.org/10.1175/1520-0469\(1984\)041<0313:TEFOTT>2.0.CO;2](https://doi.org/10.1175/1520-0469(1984)041<0313:TEFOTT>2.0.CO;2).

- Lindzen, R. S., and S. Nigam, 1987: On the role of sea surface temperature gradients in forcing low-level winds and convergence in the tropics. *J. Atmos. Sci.*, **44**, 2418–2436, [https://doi.org/10.1175/1520-0469\(1987\)044<2418:OTROSS>2.0.CO;2](https://doi.org/10.1175/1520-0469(1987)044<2418:OTROSS>2.0.CO;2).
- Ling, J., and C. Zhang, 2013: Diabatic heating profiles in recent global reanalyses. *J. Climate*, **26**, 3307–3325, <https://doi.org/10.1175/JCLI-D-12-00384.1>.
- Liu, Q., N. Wen, and Z. Liu, 2006: An observational study of the impact of the North Pacific SST on the atmosphere. *Geophys. Res. Lett.*, **33**, L18611, <https://doi.org/10.1029/2006GL026082>.
- Liu, X., P. Chang, J. Kurian, R. Saravanan, and X. Lin, 2018: Satellite-observed precipitation response to ocean mesoscale eddies. *J. Climate*, **31**, 6879–6895, <https://doi.org/10.1175/JCLI-D-17-0668.1>.
- Ma, J., H. Xu, C. Dong, P. Lin, and Y. Liu, 2015: Atmospheric responses to oceanic eddies in the Kuroshio Extension region. *J. Geophys. Res. Atmos.*, **120**, 6313–6330, <https://doi.org/10.1002/2014JD022930>.
- Ma, X., and Coauthors, 2015: Distant influence of Kuroshio eddies on North Pacific weather patterns? *Sci. Rep.*, **5**, 17785, <https://doi.org/10.1038/srep17785>.
- Maloney, E. D., and D. B. Chelton, 2006: An assessment of the sea surface temperature influence on surface wind stress in numerical weather prediction and climate models. *J. Climate*, **19**, 2743–2762, <https://doi.org/10.1175/JCLI3728.1>.
- Masunaga, R., H. Nakamura, T. Miyasaka, K. Nishii, and Y. Tanimoto, 2015: Separation of climatological imprints of the Kuroshio Extension and Oyashio fronts on the wintertime atmospheric boundary layer: Their sensitivity to SST resolution prescribed for atmospheric reanalysis. *J. Climate*, **28**, 1764–1787, <https://doi.org/10.1175/JCLI-D-14-00314.1>.
- , —, —, and B. Qiu, 2016: Interannual modulations of oceanic imprints on the wintertime atmospheric boundary layer under the changing dynamical regimes of the Kuroshio Extension. *J. Climate*, **29**, 3273–3296, <https://doi.org/10.1175/JCLI-D-15-0545.1>.
- Metz, W., 1991: Optimal relationship of large-scale flow patterns and the barotropic feedback due to high-frequency eddies. *J. Atmos. Sci.*, **48**, 1141–1159, [https://doi.org/10.1175/1520-0469\(1991\)048<1141:OROLSF>2.0.CO;2](https://doi.org/10.1175/1520-0469(1991)048<1141:OROLSF>2.0.CO;2).
- Minobe, S., A. Kuwano-Yoshida, N. Komori, S.-P. Xie, and R. J. Small, 2008: Influence of the Gulf Stream on the troposphere. *Nature*, **452**, 206–209, <https://doi.org/10.1038/nature06690>.
- Mizuno, K., and W. B. White, 1983: Annual and interannual variability in the Kuroshio Current system. *J. Phys. Oceanogr.*, **13**, 1847–1867, [https://doi.org/10.1175/1520-0485\(1983\)013<1847:AAIVIT>2.0.CO;2](https://doi.org/10.1175/1520-0485(1983)013<1847:AAIVIT>2.0.CO;2).
- Nakamura, H., T. Sampe, Y. Tanimoto, and A. Shimpo, 2004: Observed associations among storm tracks, jet streams and midlatitude oceanic fronts. *Earth's Climate: The Ocean–Atmosphere Interaction*, *Geophys. Monogr.*, Vol. 147, Amer. Geophys. Union, 329–345, <https://doi.org/10.1029/147GM18>.
- Nishii, K., H. Nakamura, and T. Miyasaka, 2009: Modulations in the planetary wave field induced by upward-propagating Rossby wave packets prior to stratospheric sudden warming events: A case-study. *Quart. J. Roy. Meteor. Soc.*, **135**, 39–52, <https://doi.org/10.1002/qj.359>.
- Nishikawa, H., I. Yasuda, and S. Itoh, 2011: Impact of winter-to-spring environmental variability along the Kuroshio jet on the recruitment of Japanese sardine (*Sardinops melanostictus*). *Fish. Oceanogr.*, **20**, 570–582, <https://doi.org/10.1111/j.1365-2419.2011.00603.x>.
- Nonaka, M., H. Sasaki, B. Taguchi, and N. Schneider, 2020: Atmospheric-driven and intrinsic interannual-to-decadal variability in the Kuroshio Extension jet and eddy activities. *Front. Mar. Sci.*, **7**, 547442, <https://doi.org/10.3389/fmars.2020.547442>.
- Ogawa, F., and T. Spengler, 2019: Prevailing surface wind direction during air–sea heat exchange. *J. Climate*, **32**, 5601–5617, <https://doi.org/10.1175/JCLI-D-18-0752.1>.
- Oka, E., and B. Qiu, 2012: Progress of North Pacific mode water research in the past decade. *J. Oceanogr.*, **68**, 5–20, <https://doi.org/10.1007/s10872-011-0032-5>.
- , and Coauthors, 2015: Decadal variability of Subtropical Mode Water subduction and its impact on biogeochemistry. *J. Oceanogr.*, **71**, 389–400, <https://doi.org/10.1007/s10872-015-0300-x>.
- , K. Yamada, D. Sasano, K. Enyo, T. Nakano, and M. Ishii, 2019: Remotely forced decadal physical and biogeochemical variability of North Pacific subtropical mode water over the last 40 years. *Geophys. Res. Lett.*, **46**, 1555–1561, <https://doi.org/10.1029/2018GL081330>.
- Okajima, S., H. Nakamura, K. Nishii, T. Miyasaka, A. Kuwano-Yoshida, B. Taguchi, M. Mori, and Y. Kosaka, 2018: Mechanisms for the maintenance of the wintertime basin-scale atmospheric response to decadal SST variability in the North Pacific subarctic frontal zone. *J. Climate*, **31**, 297–315, <https://doi.org/10.1175/JCLI-D-17-0200.1>.
- O'Reilly, C. H., and A. Czaja, 2015: The response of the Pacific storm track and atmospheric circulation to Kuroshio Extension variability. *Quart. J. Roy. Meteor. Soc.*, **141**, 52–66, <https://doi.org/10.1002/qj.2334>.
- Peng, S., W. A. Robinson, and M. P. Hoerling, 1997: The modeled atmospheric response to midlatitude SST anomalies and its dependence on background circulation states. *J. Climate*, **10**, 971–987, [https://doi.org/10.1175/1520-0442\(1997\)010<0971:TMARTM>2.0.CO;2](https://doi.org/10.1175/1520-0442(1997)010<0971:TMARTM>2.0.CO;2).
- , —, and S. Li, 2003: Mechanisms for the NAO responses to the North Atlantic SST tripole. *J. Climate*, **16**, 1987–2004, [https://doi.org/10.1175/1520-0442\(2003\)016<1987:MFTNRT>2.0.CO;2](https://doi.org/10.1175/1520-0442(2003)016<1987:MFTNRT>2.0.CO;2).
- Pierini, S., 2014: Kuroshio Extension bimodality and the North Pacific Oscillation: A case of intrinsic variability paced by external forcing. *J. Climate*, **27**, 448–454, <https://doi.org/10.1175/JCLI-D-13-00306.1>.
- Putrasahan, D. A., A. J. Miller, and H. Seo, 2013: Isolating mesoscale coupled ocean–atmosphere interactions in the Kuroshio Extension region. *Dyn. Atmos. Oceans*, **63**, 60–78, <https://doi.org/10.1016/j.dynatmoce.2013.04.001>.
- Qiu, B., and S. Chen, 2005: Variability of the Kuroshio Extension jet, recirculation gyre, and mesoscale eddies on decadal time scales. *J. Phys. Oceanogr.*, **35**, 2090–2103, <https://doi.org/10.1175/JPO2807.1>.
- , and —, 2010: Eddy–mean flow interaction in the decadal modulating Kuroshio Extension system. *Deep-Sea Res. II*, **57**, 1098–1110, <https://doi.org/10.1016/j.dsr2.2008.11.036>.
- , and —, 2011: Effect of decadal Kuroshio Extension jet and eddy variability on the modification of North Pacific intermediate water. *J. Phys. Oceanogr.*, **41**, 503–515, <https://doi.org/10.1175/2010JPO4575.1>.
- , K. A. Kelly, and T. M. Joyce, 1991: Mean flow and variability in the Kuroshio Extension from Geosat altimetry data. *J. Geophys. Res.*, **96**, 18 491–18 507, <https://doi.org/10.1029/91JC01834>.

- , N. Schneider, and S. Chen, 2007: Coupled decadal variability in the North Pacific: An observationally constrained idealized model. *J. Climate*, **20**, 3602–3620, <https://doi.org/10.1175/JCLI4190.1>.
- , S. Chen, N. Schneider, and B. Taguchi, 2014: A coupled decadal prediction of the dynamic state of the Kuroshio Extension system. *J. Climate*, **27**, 1751–1764, <https://doi.org/10.1175/JCLI-D-13-00318.1>.
- , —, and —, 2017: Dynamical links between the decadal variability of the Oyashio and Kuroshio Extensions. *J. Climate*, **30**, 9591–9605, <https://doi.org/10.1175/JCLI-D-17-0397.1>.
- , —, E. Oka, and S. Sugimoto, 2020: On the reset of the wind-forced decadal Kuroshio Extension variability in late 2017. *J. Climate*, **33**, 10813–10828, <https://doi.org/10.1175/JCLI-D-20-0237.1>.
- Révelard, A., C. Frankignoul, N. Sennéchal, Y.-O. Kwon, and B. Qiu, 2016: Influence of the decadal variability of the Kuroshio Extension on the atmospheric circulation in the cold season. *J. Climate*, **29**, 2123–2144, <https://doi.org/10.1175/JCLI-D-15-0511.1>.
- Reynolds, R. W., T. M. Smith, C. Liu, D. B. Chelton, K. S. Casey, and M. G. Schlax, 2007: Daily high-resolution-blended analyses for sea surface temperature. *J. Climate*, **20**, 5473–5496, <https://doi.org/10.1175/2007JCLI1824.1>.
- Sasaki, Y. N., and S. Minobe, 2015: Climatological mean features and interannual to decadal variability of ring formations in the Kuroshio Extension region. *J. Oceanogr.*, **71**, 499–509, <https://doi.org/10.1007/s10872-014-0270-4>.
- , —, and N. Schneider, 2013: Decadal response of the Kuroshio Extension jet to Rossby waves: Observation and thin-jet theory. *J. Phys. Oceanogr.*, **43**, 442–456, <https://doi.org/10.1175/JPO-D-12-096.1>.
- Seo, H., Y.-O. Kwon, and J.-J. Park, 2014: On the effect of the East/Japan Sea SST variability on the North Pacific atmospheric circulation in a regional climate model. *J. Geophys. Res. Atmos.*, **119**, 418–444, <https://doi.org/10.1002/2013JD020523>.
- Seo, Y., S. Sugimoto, and K. Hanawa, 2014: Long-term variations of the Kuroshio Extension path in winter: Meridional movement and path state change. *J. Climate*, **27**, 5929–5940, <https://doi.org/10.1175/JCLI-D-13-00641.1>.
- Siqueira, L., B. P. Kirtman, and L. C. Laurindo, 2021: Forecasting remote atmospheric responses to decadal Kuroshio stability transitions. *J. Climate*, **34**, 379–395, <https://doi.org/10.1175/JCLI-D-20-0139.1>.
- Smirnov, D., M. Newman, M. A. Alexander, Y.-O. Kwon, and C. Frankignoul, 2015: Investigating the local atmospheric response to a realistic shift in the Oyashio sea surface temperature front. *J. Climate*, **28**, 1126–1147, <https://doi.org/10.1175/JCLI-D-14-00285.1>.
- Su, Z., J. Wang, P. Klein, A. F. Thompson, and D. Menemenlis, 2018: Ocean submesoscales as a key component of the global heat budget. *Nat. Commun.*, **9**, 775, <https://doi.org/10.1038/s41467-018-02983-w>.
- Sugimoto, S., 2014: Interannual modulations of oceanic imprints on the wintertime atmospheric boundary layer under the changing dynamical regimes of the Kuroshio Extension. *J. Climate*, **29**, 3273–3296, <https://doi.org/10.1175/JCLI-D-15-0545.1>.
- , and K. Hanawa, 2011: Roles of SST anomalies on the wintertime turbulent heat fluxes in the Kuroshio–Oyashio confluence region: Influences of warm eddies detached from the Kuroshio Extension. *J. Climate*, **24**, 6551–6561, <https://doi.org/10.1175/2011JCLI4023.1>.
- , K. Aono, and S. Fukui, 2017: Local atmospheric response to warm mesoscale ocean eddies in the Kuroshio–Oyashio confluence region. *Sci. Rep.*, **7**, 11871, <https://doi.org/10.1038/s41598-017-12206-9>.
- Taguchi, B., S.-P. Xie, N. Schneider, M. Nonaka, H. Sasaki, and Y. Sasai, 2007: Decadal variability of the Kuroshio Extension: Observations and an eddy-resolving model hindcast. *J. Climate*, **20**, 2357–2377, <https://doi.org/10.1175/JCLI4142.1>.
- , B. Qiu, M. Nonaka, H. Sasaki, S.-P. Xie, and N. Schneider, 2010: Decadal variability of the Kuroshio Extension: Mesoscale eddies and recirculations. *Ocean Dyn.*, **60**, 673–691, <https://doi.org/10.1007/s10236-010-0295-1>.
- , H. Nakamura, M. Nonaka, N. Komori, A. Kuwano-Yoshida, K. Takaya, and A. Goto, 2012: Seasonal evolutions of atmospheric response to decadal SST anomalies in the North Pacific subarctic frontal zone: Observations and a coupled model simulation. *J. Climate*, **25**, 111–139, <https://doi.org/10.1175/JCLI-D-11-00046.1>.
- Takahashi, C., and R. Shirooka, 2014: Storm track activity over the North Pacific associated with the Madden–Julian Oscillation under ENSO conditions during boreal winter. *J. Geophys. Res. Atmos.*, **119**, 10663–10683, <https://doi.org/10.1002/2014JD021973>.
- Takaya, K., and H. Nakamura, 2001: A formulation of a phase-independent wave-activity flux for stationary and migratory quasigeostrophic eddies on a zonally varying basic flow. *J. Atmos. Sci.*, **58**, 608–627, [https://doi.org/10.1175/1520-0469\(2001\)058<0608:AFOAPI>2.0.CO;2](https://doi.org/10.1175/1520-0469(2001)058<0608:AFOAPI>2.0.CO;2).
- Tanaka, S., K. Nishii, and H. Nakamura, 2016: Vertical structure and energetics of the western Pacific teleconnection pattern. *J. Climate*, **29**, 6597–6616, <https://doi.org/10.1175/JCLI-D-15-0549.1>.
- Tang, Z., R.-H. Zhang, H. Wang, S. Zhang, and H. Wang, 2021: Mesoscale surface wind–SST coupling in a high-resolution CESM over the KE and ARC regions. *J. Adv. Model. Earth Syst.*, **13**, e2021MS002822, <https://doi.org/10.1029/2021MS002822>.
- Tomita, H., M. F. Cronin, and S. Ohishi, 2021: Asymmetric air–sea heat flux response and ocean impact to synoptic-scale atmospheric disturbances observed at JKEO and KEO buoys. *Sci. Rep.*, **11**, 469, <https://doi.org/10.1038/s41598-020-80665-8>.
- Wallace, J. M., T. P. Mitchell, and C. Deser, 1989: The influence of sea-surface temperature on surface wind in the eastern equatorial Pacific: Seasonal and interannual variability. *J. Climate*, **2**, 1492–1499, [https://doi.org/10.1175/1520-0442\(1989\)002<1492:TIOSST>2.0.CO;2](https://doi.org/10.1175/1520-0442(1989)002<1492:TIOSST>2.0.CO;2).
- , C. Smith, and C. S. Bretherton, 1992: Singular value decomposition of wintertime sea surface temperature and 500-mb height anomalies. *J. Climate*, **5**, 561–576, [https://doi.org/10.1175/1520-0442\(1992\)005<0561:SVDOWS>2.0.CO;2](https://doi.org/10.1175/1520-0442(1992)005<0561:SVDOWS>2.0.CO;2).
- Wang, Q., S.-P. Zhang, S.-P. Xie, J. R. Norris, J.-X. Sun, and Y.-X. Jiang, 2019: Observed variations of the atmospheric boundary layer and stratocumulus over a warm eddy in the Kuroshio Extension. *Mon. Wea. Rev.*, **147**, 1581–1591, <https://doi.org/10.1175/MWR-D-18-0381.1>.
- , M. Mu, and S. Pierini, 2020: The fastest growing initial error in prediction of the Kuroshio Extension state transition processes and its growth. *Climate Dyn.*, **54**, 1953–1971, <https://doi.org/10.1007/s00382-019-05097-1>.
- Wen, N., C. Frankignoul, and G. Gastineau, 2016: Active AMOC–NAO coupling in the IPSL-CM5A-MR climate

- model. *Climate Dyn.*, **47**, 2105–2119, <https://doi.org/10.1007/s00382-015-2953-y>.
- Willison, J., W. A. Robinson, and G. M. Lackmann, 2013: The importance of resolving mesoscale latent heating in the North Atlantic storm track. *J. Atmos. Sci.*, **70**, 2234–2250, <https://doi.org/10.1175/JAS-D-12-0226.1>.
- Wills, S. M., and D. W. J. Thompson, 2018: On the observed relationships between wintertime variability in Kuroshio–Oyashio Extension sea surface temperatures and the atmospheric circulation over the North Pacific. *J. Climate*, **31**, 4669–4681, <https://doi.org/10.1175/JCLI-D-17-0343.1>.
- Xu, L., P. Li, S.-P. Xie, Q. Liu, C. Liu, and W. Gao, 2016: Observing mesoscale eddy effects on mode-water subduction and transport in the North Pacific. *Nat. Commun.*, **7**, 10505, <https://doi.org/10.1038/ncomms10505>.
- Xue, J., C. Sun, J. Li, J. Mao, H. Nakamura, T. Miyasaka, and Y. Xu, 2018: Divergent responses of extratropical atmospheric circulation to interhemispheric dipolar SST forcing over the two hemispheres in boreal winter. *J. Climate*, **31**, 7599–7619, <https://doi.org/10.1175/JCLI-D-17-0817.1>.
- Yanai, M., and T. Tomita, 1998: Seasonal and interannual variability of atmospheric heat sources and moisture sinks as determined from NCEP–NCAR reanalysis. *J. Climate*, **11**, 463–482, [https://doi.org/10.1175/1520-0442\(1998\)011<0463:SAIVOA>2.0.CO;2](https://doi.org/10.1175/1520-0442(1998)011<0463:SAIVOA>2.0.CO;2).
- Yang, H., B. Qiu, P. Chang, L. Wu, S. Wang, Z. Chen, and Y. Yang, 2018: Decadal variability of eddy characteristics and energetics in the Kuroshio Extension: Unstable versus stable states. *J. Geophys. Res. Oceans*, **123**, 6653–6669, <https://doi.org/10.1029/2018JC014081>.
- Yang, Y., X. S. Liang, B. Qiu, and S. Chen, 2017: On the decadal variability of the eddy kinetic energy in the Kuroshio Extension. *J. Phys. Oceanogr.*, **47**, 1169–1187, <https://doi.org/10.1175/JPO-D-16-0201.1>.
- Yasuda, I., 2003: Hydrographic structure and variability in the Kuroshio–Oyashio transition area. *J. Oceanogr.*, **59**, 389–402, <https://doi.org/10.1023/A:1025580313836>.
- Yu, J., B. Gan, Z. Jing, and L. Wu, 2020: Winter extreme mixed layer depth south of the Kuroshio Extension. *J. Climate*, **33**, 10 419–10 436, <https://doi.org/10.1175/JCLI-D-20-0119.1>.
- Zhang, C., H. Liu, J. Xie, P. Lin, C. Li, Q. Yang, and J. Song, 2020: North Pacific storm track response to the mesoscale SST in a global high-resolution atmospheric model. *Climate Dyn.*, **55**, 1597–1611, <https://doi.org/10.1007/s00382-020-05343-x>.
- Zhang, L., B. Gan, L. Wu, W. Cai, and H. Ma, 2018: Seasonal dependence of coupling between storm tracks and sea surface temperature in the Southern Hemisphere midlatitudes: A statistical assessment. *J. Climate*, **31**, 4055–4074, <https://doi.org/10.1175/JCLI-D-17-0196.1>.
- , —, H. Wang, L. Wu, and W. Cai, 2020: Essential role of the midlatitude South Atlantic variability in altering the Southern Hemisphere summer storm tracks. *Geophys. Res. Lett.*, **47**, e2020GL087910, <https://doi.org/10.1029/2020GL087910>.
- , —, X. Li, H. Wang, C.-Y. Wang, W. Cai, and L. Wu, 2021: Remote influence of the midlatitude South Atlantic variability in spring on Antarctic summer sea ice. *Geophys. Res. Lett.*, **48**, e2020GL090810, <https://doi.org/10.1029/2020GL090810>.
- Zhuge, A., and B. Tan, 2021: The springtime western Pacific pattern: Its formation and maintenance mechanisms and climate impacts. *J. Climate*, **34**, 4913–4936, <https://doi.org/10.1175/JCLI-D-20-0051.1>.